

# Endocannabinoids disinhibit the ventral tegmental nucleus of Gudden to dorsal premammillary nucleus pathway to enhance escape behavior following learned threat experience

Received: 6 September 2024

Accepted: 13 May 2025

Published online: 27 May 2025

 Check for updates

Ruikai Chai<sup>1,6</sup>, Nawen Wang<sup>1,6</sup>, Jinlu Nie<sup>1,6</sup>, Zongyi Xu<sup>1,6</sup>, Shuqian Zhang<sup>1</sup>, Suixin Deng<sup>1</sup>, Rongxin Wang<sup>1</sup>, Mu Li<sup>1</sup>, Xinyi Gao<sup>1</sup>, Ruijie Geng<sup>2</sup>, Haibin Li<sup>2</sup>, Lei Li<sup>1</sup>, Hebi Wu<sup>1</sup>, Zhiming Li<sup>1</sup>, Tian-Lin Cheng<sup>3</sup>, Xiao-Hong Xu<sup>4</sup>, Yousheng Shu<sup>5</sup>✉, Huilin Hong<sup>1</sup>✉, Xiao Huang<sup>2</sup>✉ & Weisheng Wang<sup>1</sup>✉

Innate escape behaviors, while not requiring prior learning, are shaped by an animal's learned experiences, such as previous exposure. Here, we found that learned threat experience in mice enhances flight behaviors, which is linked to increased activation of cholecystokinin-expressing neurons in the dorsal premammillary nucleus (PMd<sup>CCK</sup> neurons), a population that controls circa-strike escape responses. This heightened activity coincides with reduced inhibition from parvalbumin-expressing GABAergic neurons in the ventral tegmental nucleus of Gudden (VTg<sup>PV</sup>), which typically suppress PMd<sup>CCK</sup> activity and escape behaviors. Furthermore, threat memory prompts a prefrontal projection to stimulate the release of endocannabinoids, inhibiting the axon terminals of VTg<sup>PV</sup> neurons. The necessity of this endocannabinoid-mediated disinhibition for the observed enhancement in flight behaviors is confirmed through genetic deletion or pharmacological blockade of endocannabinoid receptors on VTg<sup>PV</sup> neurons. Thus, our study uncovers a neural mechanism by which experience amplifies innate escape behaviors, highlighting the crucial role of endocannabinoids.

Escape behavior is essential for an animal's survival<sup>1</sup>. Due to its importance, this type of behavior is genetically hardwired in the brain without learning. Nevertheless, escape behavior undergoes dynamic adaptive changes according to the animal's experience, to balance energy expenditure and risk<sup>1</sup>. A particularly important aspect of such dynamic changes is that prior threat history strengthens the animal's vigilance<sup>2–5</sup>, leading to exaggerated flight behavior, including a lowered threshold for evading a predator,

decreased flight response time, and increased escape vigor. This strengthened vigilance could reflect the animal's recognition of increased risks in the environment due to prior encounters<sup>6</sup>, although the imminent threat is already out of sight. While the neural mechanism underlying this adaptive strengthening is not known, from a circuit perspective, this effect could be due to an experience-induced plastic change of the nuclei controlling the escape behavior.

A full list of affiliations appears at the end of the paper. ✉e-mail: [yousheng@fudan.edu.cn](mailto:yousheng@fudan.edu.cn); [hlhong1001@hotmail.com](mailto:hlhong1001@hotmail.com); [huang.xiao@zs-hospital.sh.cn](mailto:huang.xiao@zs-hospital.sh.cn); [weishengw@fudan.edu.cn](mailto:weishengw@fudan.edu.cn)

The dorsal preammillary nucleus (PMd) is a central brain region that controls the escape behavior. PMd is located in the medial hypothalamus, which is the brain region that integrates threatening predator information from different sensory modalities<sup>1,7</sup>. PMd is also the largest hypothalamic input to the dorsal periaqueductal gray (dPAG)<sup>8</sup>, which directly mediates the execution of escape behavior<sup>9,10</sup>. Our previous studies demonstrated that cholecystokinin-expressing neurons in PMd (PMd<sup>CCK</sup> neurons) exert potent control of escape vigor in multiple innate threat modalities<sup>11,12</sup>. We hypothesized that PMd<sup>CCK</sup> neurons could also be involved in the experience-induced strengthening of escape.

To test the hypothesis above, in this study, we established a behavior paradigm for experience-induced strengthening of escape. We found that learned experience of threat increases the activity of PMd<sup>CCK</sup> neurons and induces exaggerated flight behavior in mice. We further dissected a tripartite synaptic mechanism underlying this effect. PMd<sup>CCK</sup> neurons receive inputs from mPFC neurons and parvalbumin-expressing GABAergic neurons in the ventral tegmental nucleus of Gudden (VTg<sup>PV</sup>). After repeated exposure to the threat, mPFC neurons elicited an elevated endocannabinoids (eCBs) signal on the inhibitory projections between VTg<sup>PV</sup> neurons and PMd<sup>CCK</sup> neurons. This eCB signal weakens the inhibition of PMd<sup>CCK</sup> neurons, leading to strengthened escape behavior. Thus, our study revealed an mPFC/VTg to PMd circuit that controls the threat memory-driven strengthening of escape. We further demonstrated a heterosynaptic role of eCB signaling as the underlying molecular mechanism. These results have implications in understanding the neural mechanism of adaptive flexibility as well as in providing targets for modulation when such a mechanism goes awry.

## Results

### Learned threat experience induces exaggerated flights that depend on enhanced activation of PMd<sup>CCK</sup> neurons

To study whether prior threat experiences modify escape, we established a paradigm using repeated exposure to the innate fear odor 2-methyl-2-thiazoline (2MT). Using a conditioned place aversion (CPA) procedure, we assessed the learning effect of this paradigm. Mice exposed to 2MT for 5 trials (referred to as the learned group) spent significantly less time in the compartment paired with 2MT (CPA score:  $-88.81 \pm 10.43$  s;  $p < 0.001$  vs other groups). However, a single-time exposure (referred as the acute group), three-time exposure, or exposed to saline control (referred as the saline group) did not produce place aversion (Supplementary Fig. 1a, b; CPA score: acute,  $-16.52 \pm 12.56$  s; three-time,  $-18.27 \pm 14.18$  s; saline for 1 trial,  $14.46 \pm 11.76$  s; saline for 5 trials,  $-7.45 \pm 9.39$  s). These results indicated that 2MT exposure is a negative stimulus for mice, and repeated exposure leads to measurable memory of the negative experience.

We next investigated whether this memorized negative experience could influence defensive responses to innate threats. To this end, the mice were subjected to escape-inducing assays<sup>12</sup> before and after the 2MT exposure paradigm (Fig. 1a). We assessed the innate flight behaviors during two different contexts: in the rat assay, mice climbed away from an awake rat for 20 min; and in the CO<sub>2</sub> test, mice jumped in a box filled with 15% CO<sub>2</sub> for 10 min. In both assays, we quantified the escape speed and number of escape attempts and found that mice in the learned group showed exaggerated flight behaviors in both metrics across two different contexts, while mice received single-time or three-time 2MT exposure or saline showed no effect (Fig. 1b, c and supplementary Fig. 1c, d). These data demonstrated a robust strengthening of mice's innate flight responses after learned aversive experience.

We recently discovered that PMd<sup>CCK</sup> neurons play essential roles in controlling escape<sup>11,12</sup>. Thus, we hypothesized that PMd<sup>CCK</sup> neurons could be a control point mediating experience-driven modulation of innate flight behaviors. To directly test this hypothesis, we ablated

PMd<sup>CCK</sup> neurons with bilateral PMd injection of the AAV-DIO-taCaspase3 virus in CCK-Cre mice (Supplementary Fig. 1i–k) and tested the effect on learning-induced escape changes. Consistent with our previous reports<sup>12</sup>, we found that the ablation of PMd<sup>CCK</sup> neurons attenuated escape vigor and reduced the number of flights (Supplementary Fig. 1m, n), and disrupted 2MT-induced CPA behaviors (Supplementary Fig. 1l). Strikingly, PMd<sup>CCK</sup> neuron ablation blocked learning-induced strengthening of escape after repeated exposure to 2MT (Fig. 1d, e). These results indicated that PMd<sup>CCK</sup> neuron activity is necessary for learned experience-induced exaggeration of flight behaviors.

We next examined the effect of learning on the activity of PMd<sup>CCK</sup> neurons. To do this, we performed fiber photometry to measure calcium (Ca<sup>2+</sup>) dynamics of PMd<sup>CCK</sup> neurons by injecting the AAV-DIO-GCaMP7s virus into the PMd of CCK-Cre mice and implanted an optical fiber into the PMd (Fig. 1f). We were able to record GCaMP signals in PMd<sup>CCK</sup> neurons during the rat and CO<sub>2</sub> assays. We found robust activation of PMd<sup>CCK</sup> neurons around the onset of escape, consistent with our previous studies<sup>12</sup>. Importantly, these escape-related activities significantly increased in learned mice, compared to mice with single-time or saline exposure (Fig. 1j, h). These data suggested that learning induces plastic strengthening of the PMd<sup>CCK</sup> neurons that could be an underlying mechanism for the elevated flight behaviors.

### PMd<sup>CCK</sup> neurons receive afferent projections from both PFC and VTg

To dissect the circuit mechanism underlying the learning-induced strengthening of PMd<sup>CCK</sup> neurons, we next examined the synaptic inputs to these neurons. To achieve this, we used a monosynaptic retrograde tracing strategy with recombinant rabies virus (RV)<sup>13</sup> (Fig. 2a, b). We found a high percentage of retrogradely labeled neurons in the medial prefrontal cortex (mPFC) (Fig. 2c1), a region implicated in emotion regulation and cognitive control<sup>14,15</sup>. The mPFC to PMd pathway has been noted in other studies, although the function is not known<sup>16,17</sup>. In addition, PMd<sup>CCK</sup> neurons received the densest innervations from the VTg (Fig. 2c2), a region located in the medial part of the pontine tegmental area, of which the function is poorly understood<sup>18</sup>. Additional retrograde and anterograde anatomical mapping revealed that PMd<sup>CCK</sup> neurons are well-positioned as a control point for flexible defensive behaviors, as this nucleus forms connections with many brain regions related to emotional processes and defensive behaviors such as ventral subiculum (vSub)<sup>19</sup> (Fig. 2C3), hypothalamic nucleus (AHN)<sup>20,21</sup>, central amygdaloid nucleus (CeM)<sup>22</sup>, superior colliculus (SC)<sup>9</sup>, medial insular cortex (mIC)<sup>23</sup>, the dorsal periaqueductal gray (dPAG)<sup>8</sup> and more (Supplementary Fig. 2).

### VTg parvalbumin neurons directly inhibit PMd<sup>CCK</sup> neurons and control escape behavior

Our anatomical mapping results showed that the VTg which mostly consists of parvalbumin neurons and has the most robust innervations to PMd<sup>CCK</sup> neurons (Fig. 2d)<sup>24</sup>. As several recent studies have demonstrated the involvement of inhibitory modulations on defensive behaviors<sup>25–29</sup>, we hypothesized that VTg<sup>PV</sup> neurons may directly suppress PMd<sup>CCK</sup> neurons and escape behavior.

To test the hypothesis above, we first performed a more detailed characterization of the VTg<sup>PV</sup> → PMd<sup>CCK</sup> projections with PV-Cre and CCK-Cre mice. We verified our rabies tracing results of monosynaptic VTg → PMd<sup>CCK</sup> projection by injecting retrobeads in PMd (Supplementary Fig. 3a) and by injecting Retro-AAV-Flpo virus in PMd and Flpo-dependent reporter virus in VTg (Fig. 3a). In addition, we found that the VTg → PMd<sup>CCK</sup> projectors are primarily parvalbumin (PV) neurons (Fig. 3b and d, 71%), which send robust projections that thoroughly innervate PMd (Fig. 3c). To verify whether PMd is the primarily downstream of VTg<sup>PV</sup> neurons. We injected AAV-DIO-GFP into the VTg of PV-Cre mice. Compared to other regions, we found VTg<sup>PV</sup> neurons

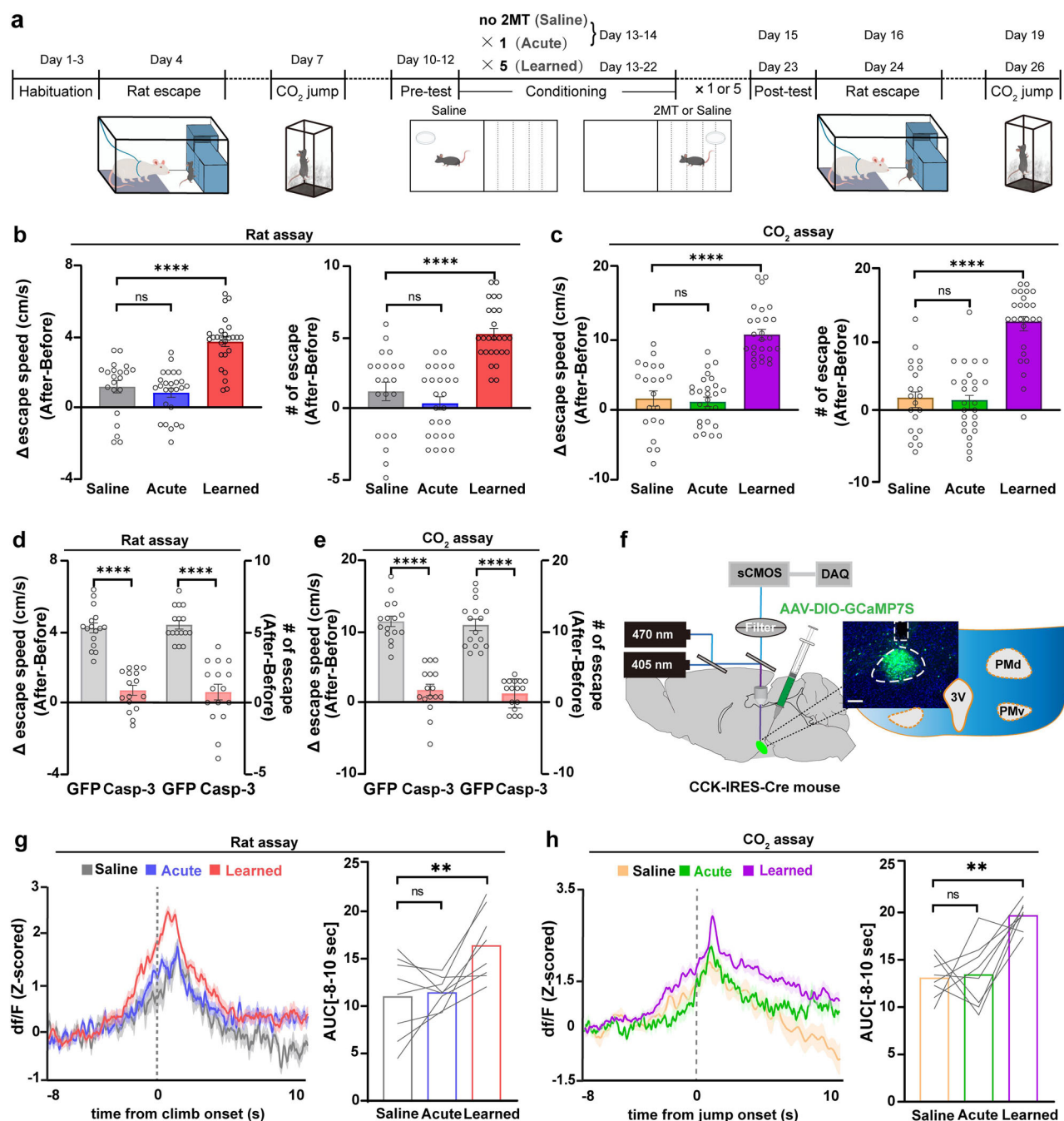


**Fig. 1 | Learned threat experience significantly increased the escape velocity, the number of flight behaviors, and the activity of PMd<sup>CK</sup> neurons.** **a** Timeline for each behavior assay. **b** Left: Repeated 2MT exposure significantly increased the escape velocity from the rat. Right: Repeated 2MT exposure significantly increased the number of escapes from the rat (Saline:  $n = 21$  mice; Acute:  $n = 26$  mice; Repeated:  $n = 26$  mice; One-way ANOVA followed by Tukey's test, \*\*\*\* $p < 0.0001$ ). **c** Left: Escape velocity for the same groups as in (b) during exposure to 15% CO<sub>2</sub>. Right: Number of jumps for the same groups in the CO<sub>2</sub> (Saline:  $n = 21$  mice; Acute:  $n = 26$  mice; Repeated:  $n = 26$  mice; One-way ANOVA followed by Tukey's test, \*\*\*\* $p < 0.0001$ ). **d** Left: Ablation of PMd<sup>CK</sup> neurons significantly impaired the velocity of exaggerated flight in rat assay. Right: Ablation of PMd<sup>CK</sup> neurons significantly decreased the number of exaggerated flight (GFP:  $n = 16$  mice; Cas-3:  $n = 16$  mice; unpaired Student's  $t$ -test, \*\*\*\* $p < 0.0001$ ). **e** Left: Ablation of PMd<sup>CK</sup> neurons significantly impaired the velocity of

exaggerated flight in CO<sub>2</sub> assay. Right: Ablation of PMd<sup>CK</sup> neurons significantly decreased the number of exaggerated flight (GFP:  $n = 16$  mice; Cas-3:  $n = 16$  mice; unpaired Student's  $t$ -test, \*\*\*\* $p < 0.0001$ ). **f** Strategy to express CGaMP7s in PMd<sup>CK</sup> neurons and the histology of GCaMP7s expression in the PMd. Scale bar, 200 μm. **g** Left: Example traces of mean escape-activated PMd<sup>CK</sup> neuron activity aligned with escape onset in mice from different groups. Right: Comparison of Z-score AUC of mice from different groups in response to rat exposure ( $n = 8$  mice for each group; One-way ANOVA followed by Tukey's test, \*\* $p < 0.01$ ). **h** Left: Neuron traces from the same groups as in (g) left during exposure to CO<sub>2</sub>. Right: Comparison of Z-score AUC in response to CO<sub>2</sub> exposure ( $n = 8$  mice for each group; One-way ANOVA followed by Tukey's test, \*\* $p < 0.01$ ). Data are presented as means  $\pm$  SEM. See also Supplementary Fig. 1. Source data are provided as a Source Data file. 2MT, 2-methyl-2-thiazoline; PMd, dorsal premammillary nucleus; PMv, premammillary nucleus, ventral part.



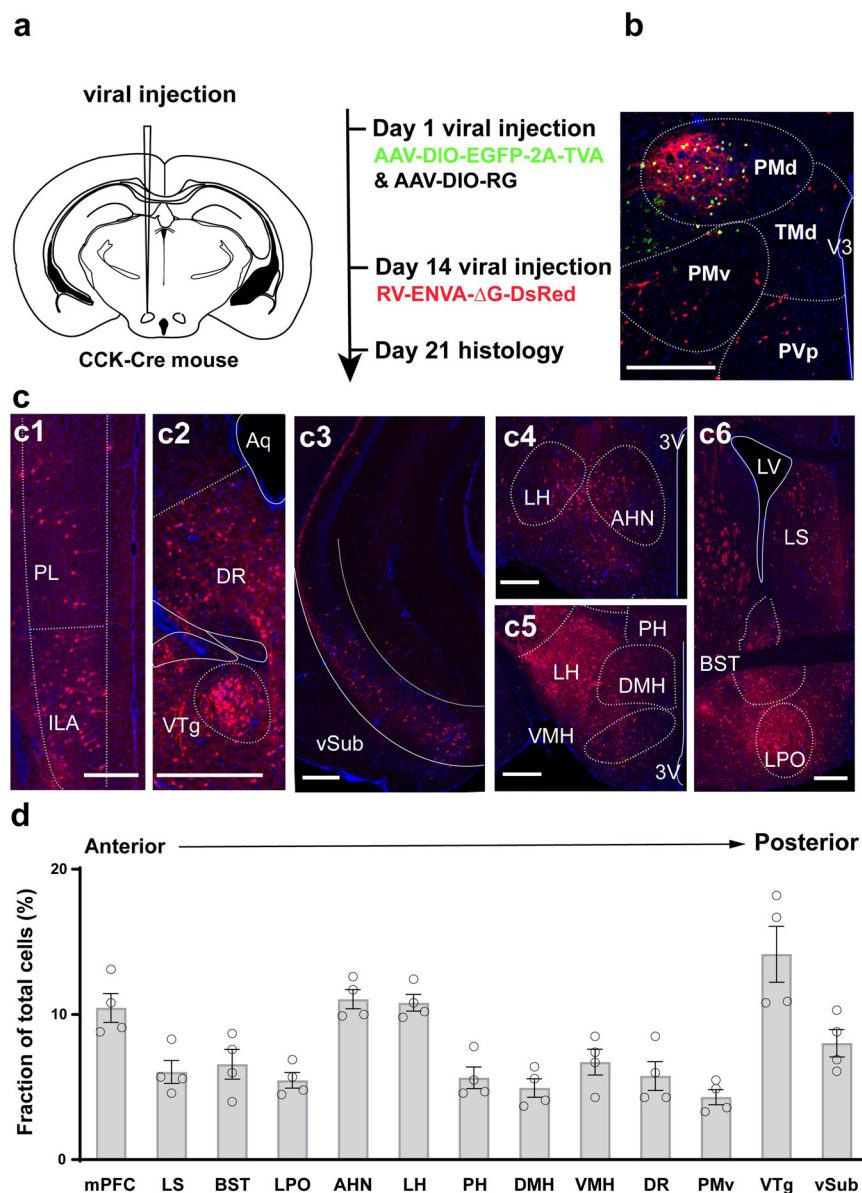


**Fig. 2 | The whole brain input of PMd<sup>CCK</sup> neurons in mice.** **a** Schematic of the pseudorabies virus tracing strategy. **b** A representative image showing PMd<sup>CCK</sup> neurons expressed with both EGFP and DsRed. Scale bar, 100  $\mu$ m. **c** Representative images showing DsRed<sup>+</sup> neurons in different brain regions, including the mPFC (c1), the DR/VTg (c2), the vSub (c3), and hypothalamic nuclei (c4–c6). Scale bar, 100  $\mu$ m. **d** Fraction of total DsRed<sup>+</sup> neurons directly projecting to PMd<sup>CCK</sup> neurons in different brain regions ( $n = 4$  mice). Data are presented as means  $\pm$  SEM. See also Supplementary Fig. 2. Source data are provided as a Source Data file. TMd,

tuberomammillary nucleus, dorsal part; PVp, paraventricular thalamic nucleus, posterior part; PL, prelimbic area; ILA, infralimbic area; DR, dorsal nucleus raphe, VTg, ventral tegmental nucleus of Gudden, vSub, ventral subiculum; LH, lateral hypothalamic area; AHN, anterior hypothalamic nucleus; PH, posterior hypothalamic nucleus; DMH, dorsomedial nucleus of the hypothalamus; VMH, ventromedial hypothalamic nucleus; 3V, 3rd ventricle; LV, lateral ventricle; LS, lateral septal nucleus; BST, bed nuclei of the stria terminalis; LPO, lateral preoptic area; mPFC, medial prefrontal cortex.

projected more strongly to the PMd and mammillary body (Supplementary Fig. 3d and e). To examine the synaptic function of VTg<sup>PV</sup>  $\rightarrow$  PMd<sup>CCK</sup> projections in a cell-type-specific manner, we took advantage of the exclusive expression of parvalbumin in VTg and cholecystikinin in PMd (Supplementary Fig. 3b and c). We were able to specifically express ChR2 in the VTg<sup>PV</sup> neurons and a GFP reporter in PMd<sup>CCK</sup> neurons, using transgenic mice that express Cre recombinase in both PV<sup>+</sup> and CCK<sup>+</sup> neurons. Again, we observed that the PMd<sup>CCK</sup> neurons were densely surrounded by VTg<sup>PV</sup> neurons' axon terminals (Fig. 3g and h), suggesting potent synaptic connections. We evaluated the functions of these connections with whole-cell patch clamp recording of PMd<sup>CCK</sup> neurons following optogenetic stimulation of ChR2-expressing VTg<sup>PV</sup> axon terminals. We observed robust negative

currents after laser stimulation, which persisted with broad blockage of excitatory channels by kynurenic acid, indicating the inhibitory nature of the synaptic transmission (Fig. 3i). This is further corroborated by the fact that these currents disappeared following tetrodotoxin application and recovered by co-treatment of potassium channel blocker 4-aminopyridine (Fig. 3i, j). Thus, these results strongly indicate that VTg<sup>PV</sup> neurons directly project to PMd to inhibit CCK-expressing neurons.

Having established that VTg<sup>PV</sup> neurons inhibit PMd<sup>CCK</sup> neurons, we next examined the function of VTg<sup>PV</sup>  $\rightarrow$  PMd<sup>CCK</sup> projections on escape behavior. To this end, we utilized the same rat assay and CO<sub>2</sub> assay described above, with selective manipulations of the VTg<sup>PV</sup>  $\rightarrow$  PMd<sup>CCK</sup> pathway. We achieved chemogenetic manipulations by injecting

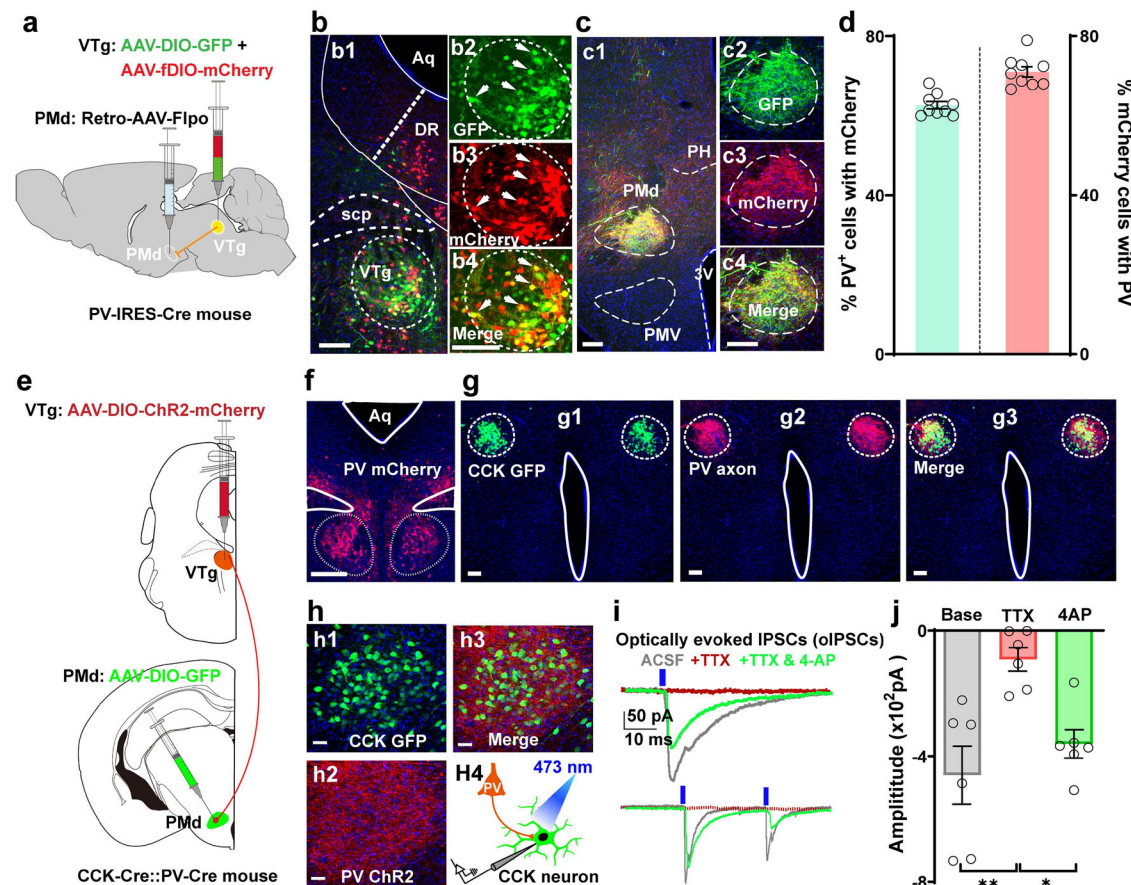


**Fig. 3 | The VTg nucleus sends monosynaptic inhibitory inputs to PMd<sup>CCK</sup> neurons.** **a** Scheme showing the approach to label VTg parvalbumin neurons projecting to the PMd. **b** A representative image showing the expression of both EGFP and mCherry in VTg<sup>PV</sup> neurons (b1). EGFP expression in VTg<sup>PV</sup> neurons (b2); Presynaptic PMd-projecting VTg neurons with mCherry (b3); Overlay (b4). Left, scale bar, 150  $\mu$ m; right, scale bar, 200  $\mu$ m. **c** Photograph showing EGFP<sup>+</sup> synaptic terminals of VTg<sup>PV</sup> neurons in the PMd (c1). EGFP<sup>+</sup> synaptic terminals of VTg<sup>PV</sup> neurons in the PMd (c2); mCherry<sup>+</sup> axon terminals of PMd-projecting VTg neurons in the PMd (c3); Overlay (c4). Left, scale bar, 150  $\mu$ m; right, scale bar, 200  $\mu$ m. **d** Quantification of overlap between PMd-projecting and PV-Cre expressing neurons (N = 4 mice; n = 9 slices). **e** Scheme showing the strategy used to label VTg<sup>PV</sup> and PMd<sup>CCK</sup> neurons in the CCK-IRES-Cre::Pvalb-IRES-Cre mouse. **f** A representative image showing the expression of mCherry in VTg<sup>PV</sup> neurons. Scale bar, 100  $\mu$ m. **g** Representative images showing

the expression of both EGFP and mCherry in the PMd. EGFP expression in PMd<sup>CCK</sup> neurons (g1); Axon terminals of PMd-projecting VTg neurons with mCherry (g2); Overlay (g3). Scale bar, 200  $\mu$ m. **h** 40x times magnified view of histology in (g). Scale bar, 50  $\mu$ m. **i** PMd CCK neuron shown in (h1) showed an inhibitory response following blue light delivery to excite ChR2-expressing VTg PV axon terminals (h2) in an ex vivo slice preparation with kynurenic acid (h4). The response disappeared following the application of tetrodotoxin (TTX, 0.3  $\mu$ M), and the response was rescued following the application of the potassium channel blocker (4-AP, 0.5 mM) in both single pulse (top) and pair pulse (bottom). **j** Quantification of the PMd<sup>CCK</sup> responses to stimulation of VTg PV terminals in (i). (N = 4 mice; n = 6 cells; One-way ANOVA followed by Tukey's test, \*p < 0.05, \*\*p < 0.01). Scale bar, 0.5  $\mu$ m. Data are presented as means  $\pm$  SEM. See also Supplementary Fig. 3. Source data are provided as a Source Data file. Aq, aqueduct; PV, parvalbumin; CCK, cholecystokinin; ACSF, the normal artificial cerebrospinal fluid; TTX, tetrodotoxin; 4-AP, 4-aminopyridine.

retrograde AAV with Cre-inducible expression of Flpo (Retro-AAV-DIO-Flpo) into the PMd of PV-Cre mice and another AAV with Flpo-dependent expression of HM3Dq, HM4Di or mCherry in VTg (Supplementary Fig. 4a, d). For optogenetic manipulations, we expressed channelrhodopsin-2 (ChR2), anion channelrhodopsin-2 (GtACR2), or control fluorescent proteins in VTg<sup>PV</sup> neurons and delivered blue light (473 nm) to axon terminals in the PMd (Supplementary Fig. 4b and g). While the excitation or inhibition of the VTg<sup>PV</sup>  $\rightarrow$  PMd<sup>CCK</sup> projections did not affect locomotion (data not shown), we observed potent control of the escape behaviors in naïve mice in the two assays (Supplementary Fig. 4). Chemogenetic or optogenetic activation of VTg<sup>PV</sup>  $\rightarrow$  PMd<sup>CCK</sup> pathway reduced the velocity and number of innate flight behaviors, while inhibition led to increases (Supplementary Fig. 4). These data demonstrated control of escape behaviors by the VTg<sup>PV</sup>  $\rightarrow$  PMd<sup>CCK</sup> pathway. Thus, regulation of the VTg<sup>PV</sup> neuron activities is sufficient in modulating the flight behaviors.

We next investigated whether changes in the VTg<sup>PV</sup>  $\rightarrow$  PMd<sup>CCK</sup> neuron activities are involved in learning-induced flight exaggeration.

We recorded GCaMP7s calcium signals of VTg<sup>PV</sup> axons in PMd using fiber photometry in mice during the escape assays (Fig. 4a). In learned mice, we found a sharp suppression of calcium activities in the terminals of VTg<sup>PV</sup> neurons that was temporally locked around the onset of flight behavior (Fig. 4b, c). Interestingly, the same pattern of activity was not observed in naïve mice, or mice with single exposure (Fig. 4b, c). To investigate the activity of VTg<sup>PV</sup> neurons, the AAV-DIO-GCaMP7s was injected into VTg of PV-Cre mice. The fluorescence signal at VTg was recorded using fiber photometry during strengthened escape behavior. We found that the calcium activities in VTg<sup>PV</sup> neurons did not show any changes during escape behavior (Fig. 4e, f). In light of our above results that inhibition of VTg<sup>PV</sup>  $\rightarrow$  PMd<sup>CCK</sup> pathway led to enhanced escape behaviors (Supplementary Fig. 4), these data suggest that threat memory could engage a suppression of VTg<sup>PV</sup>  $\rightarrow$  PMd<sup>CCK</sup> pathway to achieve escape adaptation. We further tested the necessity of VTg<sup>PV</sup>  $\rightarrow$  PMd<sup>CCK</sup> pathway suppression for threat memory-induced escape strengthening using the same virus strategies and escape assays (Fig. 4g, i). We found that activation of VTg<sup>PV</sup>  $\rightarrow$  PMd<sup>CCK</sup> pathway,



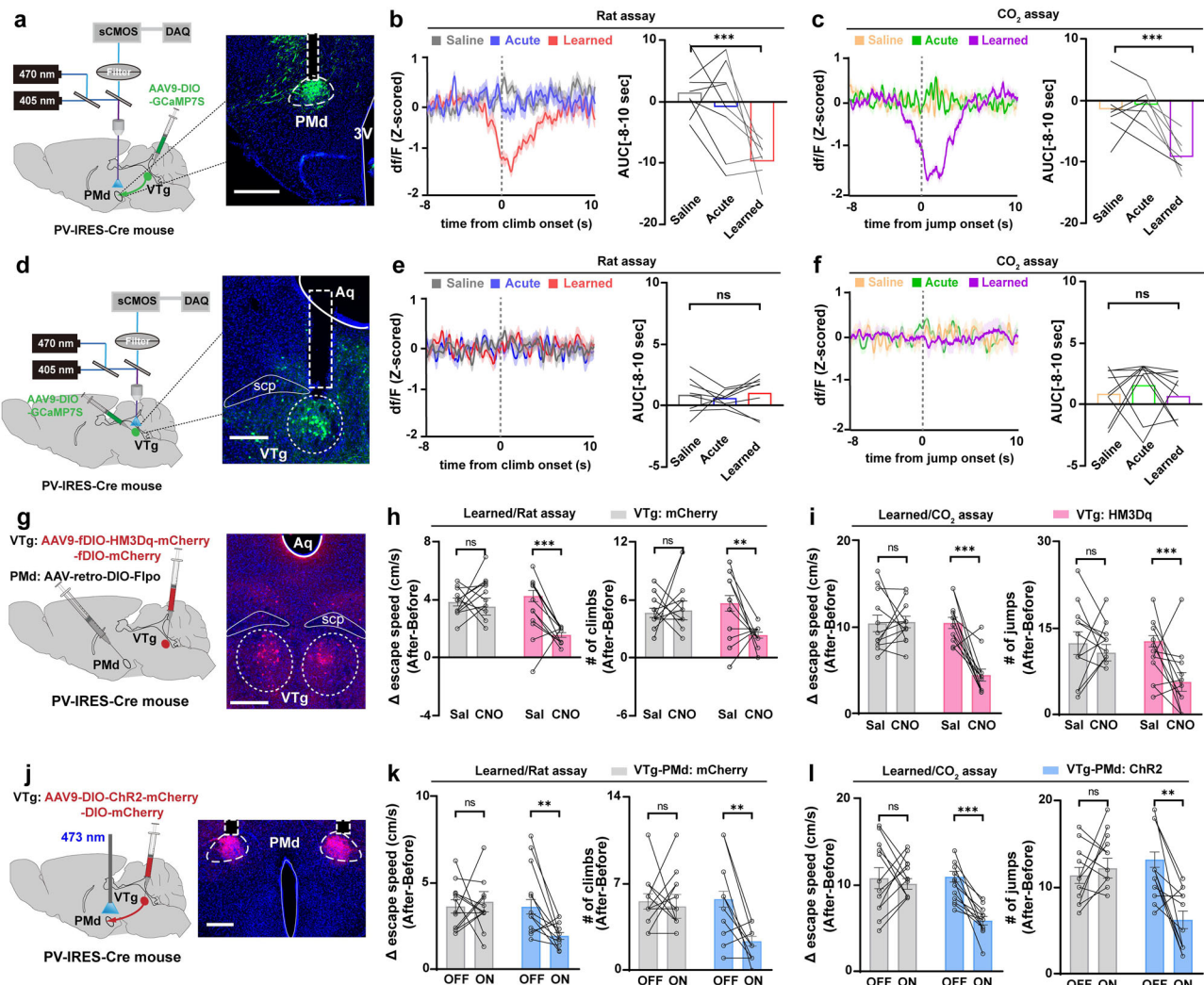


**Fig. 4 | The VTg<sup>PV</sup> neuron → PMd projection mediates exaggerated escape behaviors.** **a** Recordings were obtained from GCaMP7s-expressing VTg<sup>PV</sup> axons terminating in the PMd. Scale bar, 300  $\mu$ m. **b, c** Left: example fiber photometry traces from VTg<sup>PV</sup> axons in the PMd from the rat (**b**) and CO<sub>2</sub> assays (**c**). Right: comparison of Z-score AUC from (**b**, left) and (**c**, left) during escape; AUC, the area under the curve. ( $n = 8$  mice for each group; One-way ANOVA followed by Tukey's test, \*\*\* $p < 0.001$ ). **d** Recordings were obtained from GCaMP7s-expressing VTg<sup>PV</sup> neurons. Scale bar, 300  $\mu$ m. **e, f** Left: example fiber photometry traces from VTg<sup>PV</sup> neurons from the rat (**e**) and CO<sub>2</sub> assays (**f**). Right: comparison of Z-score AUC from (**e**, left) and (**f**, left) during escape; AUC, the area under the curve. ( $n = 8$  mice; **e**,  $n = 8$  mice; **f**,  $n = 9$  mice; One-way ANOVA followed by Tukey's test,  $p > 0.05$ ). **g** Scheme showing the strategy used to express HM3Dq in PMd-projecting VTg<sup>PV</sup> neurons (left). A representative image showing the expression of mCherry in PMd-projecting VTg<sup>PV</sup> neurons (right). Scale bar, 300  $\mu$ m. **h, i** Chemogenetic PMd-projecting VTg<sup>PV</sup> neuron excitation decreased the escape velocity (left) and the number (right) of flight behaviors in both rat (**h**) and CO<sub>2</sub> assays (**i**). (mCherry,  $n = 12$  mice; HM3Dq,  $n = 12$  mice; two-way repeated-measures ANOVA followed by Sidak's test, \*\* $p < 0.01$ ). **j** Strategy to optogenetically excite ChR2-expressing VTg<sup>PV</sup> neuron axons terminating in the PMd (left). A representative image showing the axon terminals of PMd-projecting VTg<sup>PV</sup> neurons (right). Scale bar, 200  $\mu$ m. **k, l** Optogenetic excitation of the VTg<sup>PV</sup> neuron/PMd projection with blue light (473 nm) decreased the escape velocity (left) and the number (right) of flight behaviors in both assays. (mCherry,  $n = 16$  mice; ChR2,  $n = 16$  mice; two-way repeated-measures ANOVA followed by Sidak's test, \*\* $p < 0.01$ , \*\*\* $p < 0.001$ ). Data are presented as means  $\pm$  SEM. See also Supplementary Fig. 4. Source data are provided as a Source Data file. scp, superior cerebellar peduncles.

either with chemogenetic (Fig. 4h, i) or optogenetic (Fig. 4k, l) approaches, blocked elevated escape behaviors after repeated exposure to 2MT. Together, these data indicate that the VTg<sup>PV</sup>→PMd<sup>CK</sup> projection is a direct control for flight behavior that is necessary for threat history induced escape adaptation.

### eCB system controls plasticity at VTg→PMd synapses and behavioral adaptation

Our above data indicated a suppression of inhibitory VTg<sup>PV</sup> → PMd<sup>CK</sup> pathway controls escape adaptation with learned threat experience, thus we next tried to determine the neural mechanism underlying this plasticity. We first measured the effect of single or five-time 2MT exposure conditioning on VTg<sup>PV</sup> neurons' excitability (Supplementary Fig. 5a) and found no difference among groups (Supplementary

Fig. 5b–f). These data suggest that learning-induced suppression of VTg<sup>PV</sup> neurons does not affect their excitability at the somatic level, but could be due to changes at the VTg<sup>PV</sup> → PMd<sup>CK</sup> synapses. Since eCB signaling has been previously described as a heterosynaptic inhibitory signal<sup>30–32</sup> and a previous study demonstrated that the innervation of endocannabinoid receptor (CB<sub>1</sub>R)-containing axons was found in the PMd using immunoelectron microscopy<sup>33</sup>, we hypothesized that the endocannabinoid (eCB) system may be mediating the heterosynaptic regulation on VTg<sup>PV</sup> → PMd<sup>CK</sup> synapses. And consistent with our hypothesis, data from Allen Brain Atlas show that VTg neurons express CB<sub>1</sub>R mRNA at high levels ([www.brain-map.org](http://www.brain-map.org), Supplementary Fig. 5g). By using immunostaining, we confirmed the CB<sub>1</sub>R expression on VTg<sup>PV</sup> neurons (Supplementary Fig. 5k–n).

To further test whether the eCB released at the VTg-PMd synapses was related to repeated threat exposure, we then measured the eCB signal during escape behavior in mice with single or repeated 2MT conditioning (Fig. 5a). Using a genetically encoded GPCR activation-based eCB biosensor (GRAB<sub>eCB2.0</sub>)<sup>34–39</sup>, we found that the eCB signal showed no change related to escape behavior in mice exposed with saline or single-time 2MT, but showed a marked activation around the escape onset in mice with repeated 2MT exposure (Fig. 5b, c). This pattern matched perfectly with the plastic changes in the VTg-PMd synapses we observed (Fig. 4).

The above data established spatial-temporal proximity of eCB signal elevation and VTg-PMd synaptic suppression, we next aimed to test whether there is a causal effect. To this end, we utilized a CB<sub>1</sub>R antagonist AM251 to block the eCB signal, and recorded the calcium activity at the VTg-PMd synapses (Fig. 5d). Consistent with our previous results (Fig. 4), we observed learning-induced suppression of GCaMP signals around escape onset in both escape assays in the vehicle group. In contrast, in mice that received local injection of AM251, this learning-induced plasticity was significantly suppressed (Fig. 5e, f), indicating the necessity of an eCB signal. To further examine the impact of locally blocking eCB signal on escape adaptation, we delivered AM251 bilaterally at PMd (1 µg in 0.4 µl each side, Fig. 5g). We found that infusion of AM251 blocked escape strengthening from repeated 2MT exposure in both escape assays, and the escape behavior in naïve mice was not affected (Fig. 5h, i).

To suppress the eCB signal specifically in the VTg<sup>PV</sup>-PMd pathway, we employed the CRISPR/Cas9 knockout strategy for local ablation of CB<sub>1</sub>R at VTg<sup>PV</sup>-PMd synapses (Supplementary Fig. 5h), by injecting the AAV-gRNAs-EGFP into VTg of PV<sup>Cre</sup>::Cas9<sup>fl</sup> mice. This strategy led to the effective reduction of CB<sub>1</sub>R mRNA in the PMd region (Supplementary Fig. 5i), and we further confirmed the reduction of CB<sub>1</sub>R expression specifically on PMd-projecting axons from VTg<sup>PV</sup> neurons with immunostaining (Fig. 5j, k). Deletion of CB<sub>1</sub>R in the VTg<sup>PV</sup> neurons did not affect baseline escape behavior or negative emotions associated with 2MT exposure (Supplementary Fig. 5j). And strikingly, learning-induced exaggeration of flight behaviors in both rat and CO<sub>2</sub> assays was blocked in mice received gRNA, but not in the control group with scrambled sequences (Fig. 5k, l). Taken together, these data indicate that repeated threat exposure induces eCB release at VTg-PMd synapses to control behavioral adaptation.

### mPFC releases eCB at VTg-PMd synapses with repeated threat exposure

Given that eCBs are synthesized in the dendritic spine on demand, and this postsynaptic generation involving the action of phospholipase C requires the activation of G-protein-coupled receptors (GPCRs)<sup>40</sup>. From our anatomy results (Fig. 2), the mPFC and vSub are likely to provide excitatory inputs to PMd<sup>CK</sup> neurons, which have been implicated in behavioral regulation. To search for learning-induced plastic changes in the inputs of the PMd<sup>CK</sup> neurons, we measured c-fos expression after escape assays and compared the effect of single-time versus repeated exposure to 2MT (Fig. 6a). We found that the expression of c-fos induced by the rat escape assays in PMd was enhanced in learned mice, but not in mice with single-time or saline exposure (Fig. 6b). This is consistent with the elevated calcium responses that we recorded (Fig. 1), indicating a learning effect. Among the identified inputs of PMd<sup>CK</sup> neurons, we observed the same learning effect only in mPFC, but not in vSub (Fig. 6b and c). Considering previous reports on mPFC functions in top-down control over escape behaviors<sup>41,42</sup>, the data strongly imply that the strengthening of mPFC→PMd pathway may participate in learned threat history-induced exaggeration of escape behavior.

To directly test whether the activation of mPFC could increase eCB levels at VTg<sup>PV</sup>-PMd synapses, we injected AAV-DIO-eCB2.0 virus into the VTg of PV-Cre mice and recorded fluorescence signal at PMd

using fiber photometry. At the same time, we labeled PMd-projecting mPFC neurons with red-shifted excitatory opsin ChrimsonR or tdTomato (Fig. 6d). We used the same optic fiber to deliver 20 Hz red light (615 nm) to stimulate the axon terminals of mPFC neurons in the PMd, and simultaneously record the changes in the eCB signal at VTg<sup>PV</sup>-PMd synapses. Optogenetic activation led to a robust increase in the eCB signal, but not in the control (Fig. 6e–g). These results support our hypothesis that activation of mPFC→PMd pathway could lead to the elevation of eCB at the VTg-PMd synapses. In addition, the level of eCB increase (Fig. 5) was comparable to that induced by optogenetic activation of mPFC. To clarify whether the mPFC activation is necessary for eCB production during exaggerated flight. We injected AAV-retro-Flopo into PMd, AAV-fDIO-HM4Di or -mCherry into mPFC and AAV-DIO-eCB2.0 into VTg of PV-Cre mice and implanted an optical fiber into the PMd. We found that inhibition of PMd projecting mPFC neurons significantly blocked the increased eCB signal in learned mice (Fig. 6h–j). These data indicate that learned threat experience could induce mPFC to release eCB at VTg-PMd synapses.

### Inhibition of mPFC → PMd pathway impairs the escape adaptation

To directly test the causal role of mPFC→PMd pathway in learning-induced escape adaptation, we performed chemogenetic inhibition of the mPFC→PMd projectors by injecting a non-toxic rabies virus (RV)-Cre in the PMd and Cre-dependent mCherry or DREADD (designer receptors exclusively activated by designer drugs) viruses in mPFC (Fig. 7a). The DREADD constructs allowed us to control neuron activity by injecting Clozapine-N-oxide (CNO) in mice<sup>43,44</sup>. In naïve mice, chemogenetic activation of mPFC→PMd pathway did not affect the escape velocity and number of flights assessed in the rat assay or CO<sub>2</sub> assay (Fig. 7b, c, Supplementary Fig. 6a and b). To examine the involvement of mPFC→PMd pathway in escape adaptation, we employed repeated exposure to the 2MT paradigm described above and chemogenetically inhibited the mPFC→PMd pathway during the post-learning escape behavior tests (Fig. 7d, Exp I). We found that chemogenetic inhibition of PMd-projecting mPFC neurons significantly decreased the learning-induced exaggeration of escape behaviors in both assays (Fig. 7e, f and Supplementary Fig. 6), indicating a necessary role of mPFC→PMd pathway in the expression of learned threat history-induced escape adaption.

We further examined the involvement of mPFC→PMd pathway in the acquisition of the learned threat, by additionally inhibiting mPFC→PMd projectors during the repeated exposure to 2MT (Fig. 7d, Exp II). We found that injection of CNO during 2MT exposure blocked learning-induced strengthening of flight behaviors in all mice, even in those receiving saline during the test assays (Fig. 7e, f), indicating that mPFC→PMd pathway is necessary for the learning of the threat history. Consistent with this view, we found that chemogenetic activation or inhibition of mPFC→PMd pathway bidirectionally controls the CPA score during repeated exposure to 2MT (Supplementary Fig. 6h, i). These data indicate that mPFC→PMd pathway is necessary for learned threat history-induced escape adaption, and the activation of this pathway is important during threat exposure as well as subsequent expression of escape flexibility. Altogether, these results demonstrated a tripartite mPFC/VTg<sup>PV</sup>→PMd<sup>CK</sup> synapses that utilize eCB signal for heterosynaptic plasticity to control escape adaptation due to learned aversive memory (Fig. 7g).

### Discussion

Prior threat experience heightened the animal's sensitivity to future predator threats and enhanced the escape behavior. This capability is crucial for survival in dynamic contingencies fraught with danger, enabling animals to escape from threats at the earliest opportunity. We demonstrated here that PMd<sup>CK</sup> neurons orchestrate a tripartite circuit mediating prior learned threat-driven behavioral adaptation.



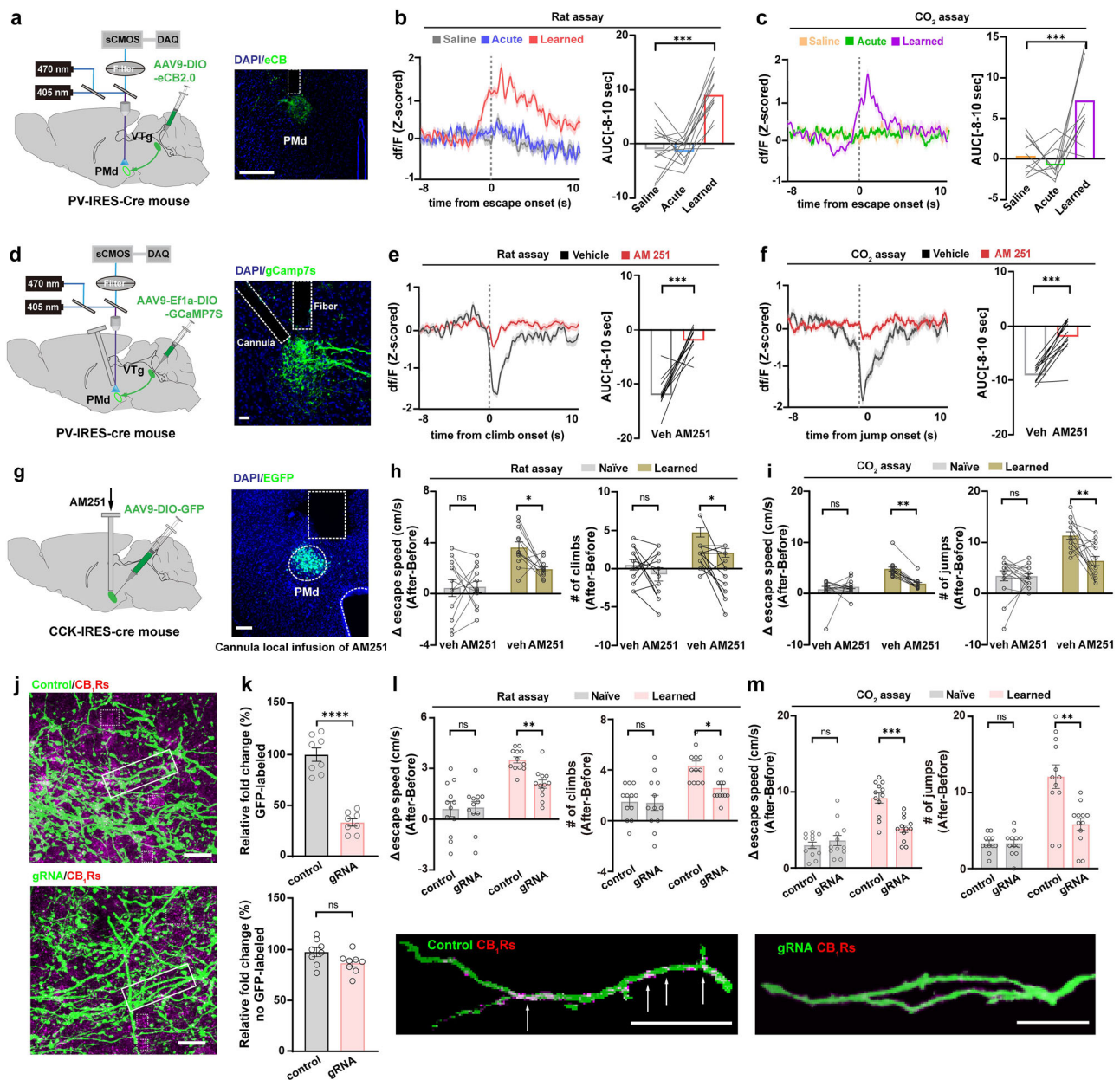


**Fig. 5 | Loss-of-function of CB<sub>1</sub>R at VTg<sup>PV</sup> → PMd synapses rescues the decreased eCB signal and impairs the exaggerated escape.** **a** Schematic diagram of eCB signal recordings. Scale bar, 400  $\mu$ m. **b, c** Left: example eCB signal in the rat (**b**) and CO<sub>2</sub> assays (**c**). Right: summarized Z-score AUC from (**b**, left) and (**c**, left). ( $n = 13$  mice for each group; One-way ANOVA followed by Tukey's test, \*\*\* $p < 0.001$ ). **d** Schematic (left), representative images of virus expression, and fiber implantation (right). Scale bar, 100  $\mu$ m. **e, f** Left: example fiber photometry traces from VTg<sup>PV</sup> axons from the rat (**e**) and CO<sub>2</sub> assays (**f**). Right: summarized Z-score AUC from (**e**, left) and (**f**, left); ( $n = 12$  mice for each group; Student t-test, \* $p < 0.05$ ). **g** Drug infusion sites were verified by expression of GFP. Scale bar, 150  $\mu$ m. **h, i** Effects of AM251 (1  $\mu$ g, 100  $\mu$ l each side) on the velocity (left) and number of escapes (right) in both rat (**h**) and CO<sub>2</sub> (**i**) assays. (**h**, Veh,  $n = 12$  mice; AM251,  $n = 12$  mice; **i**, Veh,  $n = 15$  mice; AM251,  $n = 15$  mice; two-way repeated-measures ANOVA followed by Sidak's test, \* $p < 0.05$ , \*\* $p < 0.01$ ). **j** CB<sub>1</sub>R expression in PMd after control (top)/gRNA

(bottom) virus injection in VTg of PV<sup>Cre</sup>; Cas9fl mice. Scale bar, 50  $\mu$ m; **k** Quantification of CB<sub>1</sub>R expression in VTg<sup>PV</sup> axons in the PMd ( $N = 4$  mice,  $n = 8$  axons) Student t-test, \*\*\*\* $p < 0.0001$ . **l** Top, effects of gRNA on the velocity (left) and the number (right) of flight behaviors in the rat assay. (Control,  $n = 12$  mice; gRNA,  $n = 12$  mice; two-way repeated-measures ANOVA followed by Sidak's test, \* $p < 0.05$ , \*\* $p < 0.01$ , \*\*\* $p < 0.001$ ). Bottom, representative images of axons protruding from the VTg<sup>PV</sup> neurons with CB<sub>1</sub>R expression in control group. Scale bar, 5  $\mu$ m. **m** Top, velocity and numbers of jump for the same groups as in (**l**) during exposure to CO<sub>2</sub> (two-way repeated-measures ANOVA followed by Sidak's test, \*\*\* $p < 0.001$ ,  $n = 12$  mice). Bottom, representative images of axons protruding from the VTg<sup>PV</sup> neurons without CB<sub>1</sub>R expression in gRNA group. Data are presented as means  $\pm$  SEM. See also Supplementary Fig. 5. Source data are provided as a Source Data file. eCB, endocannabinoids; CB<sub>1</sub>R, endocannabinoid receptor.

In brief, our results suggest that activation of mPFC neurons promotes exaggerated escape behavior by inducing heterosynaptic, endocannabinoid-dependent depression of VTg synaptic transmission to the PMd (Fig. 7g).

The VTg is located in the medial part of the pontine tegmental area, providing a very dense input to the PMd<sup>CK</sup> neurons (Fig. 2) that

are essential for escape behavior<sup>11,12</sup>. The functional role of the VTg was poorly understood, despite several previous lesion studies suggesting a role in modulating vigilance states and context memory<sup>45–47</sup>. Applying optogenetic control of VTg<sup>PV</sup> neurons, we showed that this nucleus controls the escape behavior. Fiber photometry recording of the calcium activity from VTg<sup>PV</sup> neurons indicated a learning-induced



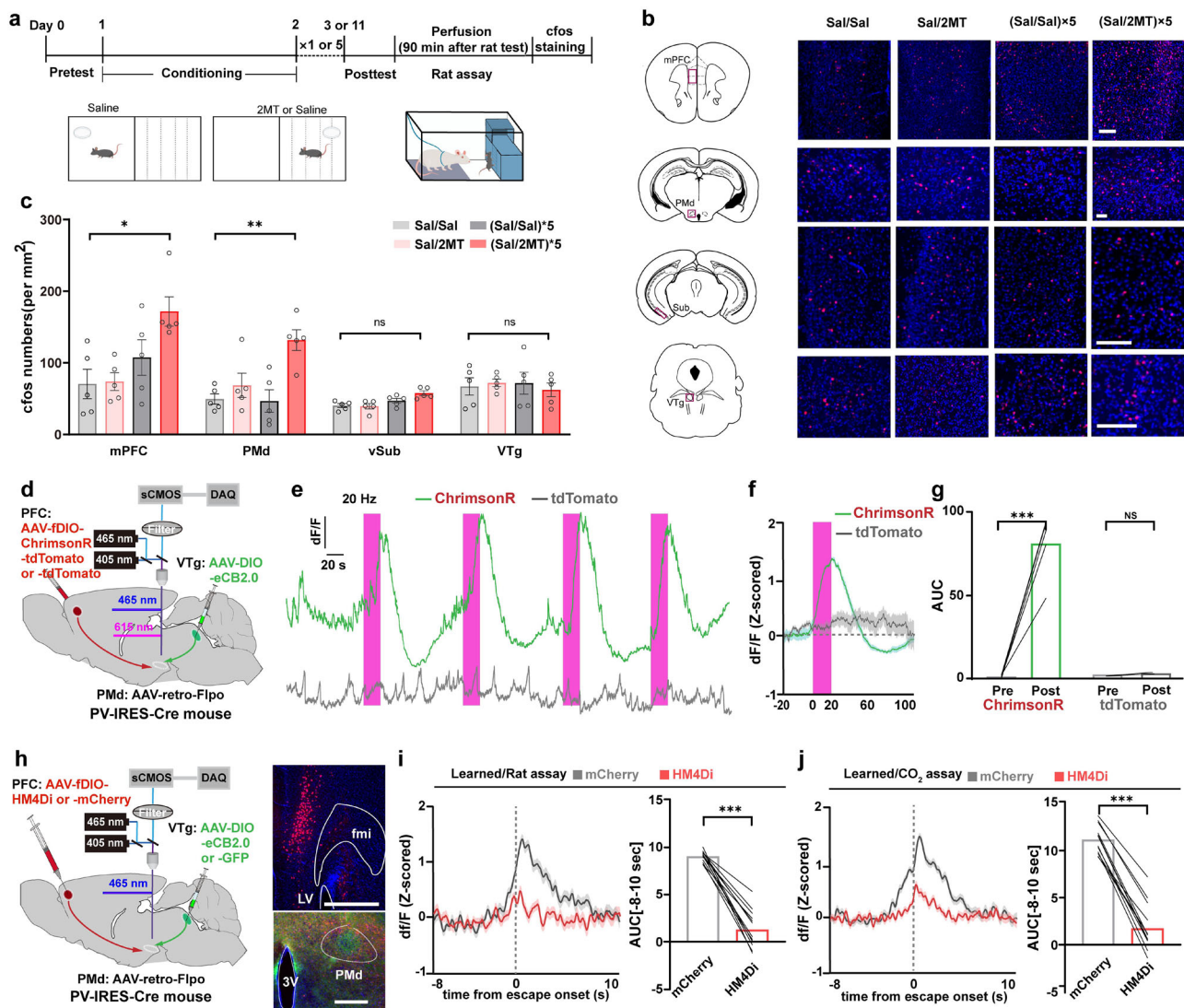


**Fig. 6 | The mPFC → PMd circuit is necessary for learning threat history-induced eCB signal increases.** **a** Schematic diagram of the experimental design for c-fos staining. **b** Images show mPFC, PMd, vSub, and VTg sections stained with antibodies against c-fos in different group mice. Scale bar, 20  $\mu$ m. **c** Rat exposure increased c-fos in mPFC and PMd, but not in vSub and VTg ( $n = 5$  mice, One-way ANOVA followed by Tukey's test,  $*p < 0.05$ ,  $**p < 0.01$ ). **d** Left: scheme showing that the fiber photometry recordings were conducted to simultaneously record changes in eCB signal and stimulate mPFC neurons axon terminals in the PMd. **e** Sample trace of eCB sensor (GRAB-eCB2.0) in the PMd in response to optogenetic excitation of axon terminals of PMd projecting mPFC neuron (20 Hz, 20 s). **f** Average traces of the change in eCB2.0 fluorescence in **(e)**. **g** Summarized Z-score AUC from

**(f)** during optogenetic stimulation. ( $n = 5$  mice, Student t-test,  $***p < 0.001$ ). **h** Left: Scheme showing that the fiber photometry recordings were conducted to record changes in eCB signal and inhibit PMd-projecting mPFC neurons. Right: Representative images showing the expression of mCherry in PMd-projecting mPFC neurons (top). The neuron axon terminals (red) and the eCB sensor (green) are in the PMd (bottom). Top, scale bar, 500  $\mu$ m; bottom, 50  $\mu$ m. **i, j** Left: example eCB signal from VTg neuron axons in the PMd from the rat **(i)** and CO<sub>2</sub> assays **(j)**. Right: summarized Z-score AUC from **(i)**, left and **(j)**, left during escape. ( $n = 13$  mice for each group; One-way ANOVA followed by Tukey's test,  $***p < 0.001$ ). Data are presented as means  $\pm$  SEM. Source data are provided as a Source Data file. Sal, saline; fmi, forceps minor of the corpus callosum.

suppression, suggesting the existence of a baseline level of VTg<sup>PV</sup> neuron activation in naïve mice. Modulating the levels of these activities provides an ideal control point to fine-tune the strength of the innate escape response. Indeed, we found that mPFC controls threat history-induced exaggerated flight behaviors by suppressing the activity of the axon terminals of VTg<sup>PV</sup> neurons to activate the PMd<sup>CK</sup> neurons. Thus, our findings establish a crucial function of the VTg neurons in regulating the strength of the escape response. Whether other cell types in VTg, or other modes of modulation on VTg neuron activity, could mediate distinct forms of experience-induced flight adaptation, such as habituation<sup>29</sup> requires further investigations. Furthermore, consistent with previous reports of a top-down modulatory role of mPFC<sup>48–53</sup> primarily using Pavlovian conditioning<sup>54</sup>, we provide the evidence that mPFC modulates learning-induced innate escape

behavior adaptation, and extend the understanding of the functions of mPFC projection to hypothalamic regions.

We discovered that mPFC modulates the strength of the VTg-PMd synapses via the endocannabinoids (eCBs) system. As a synaptic retrograde messenger, eCB suppresses neurotransmitter release by activating the presynaptic cannabinoid type 1 (CB<sub>1</sub>) receptors, which has been previously described as a modulator at inhibitory synapses<sup>30–32</sup>. In previous studies, the activation of eCB system is a neurobiological mechanism for attenuating anxiety<sup>55</sup> and learned freezing behavior<sup>50,56,57</sup>, indicating that endocannabinoids have anxiolytic and antipsychotic effects with low-imminence threats<sup>58–60</sup>. However, a recent study demonstrated that elevating the level of eCB in the amygdala strengthened innate fear-induced freezing behavior<sup>61</sup>. Similarly, pharmacological enhancement of eCB signaling increased flight

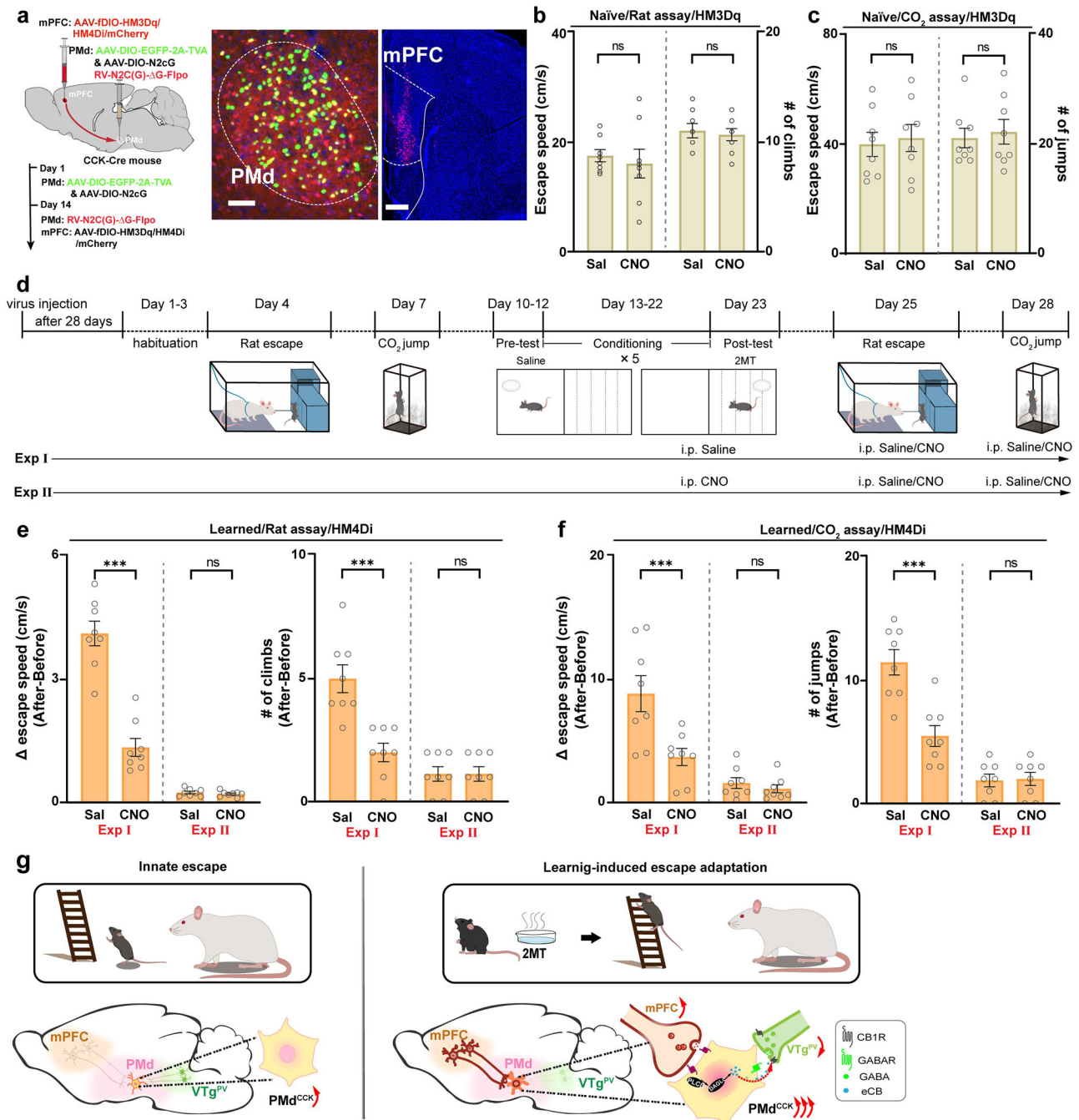


**Fig. 7 | PMd<sup>CCK</sup>-projecting mPFC neurons are necessary for learning-induced escape adaptation.** **a** Left: scheme showing the strategy used to express DREADD or mCherry in PMd<sup>CCK</sup>-projecting mPFC neurons. Representative images showing the expression of mCherry in PMd<sup>CCK</sup>-projecting mPFC neurons (Middle) and the neuron axon terminals in the PMd (Right). Middle, scale bar, 1 mm; Right, 150  $\mu$ m. **b** Chemogenetic excitation of PMd<sup>CCK</sup>-projecting mPFC neuron did not affect the escape velocity and the number of escapes in naïve mice from live rat (Saline,  $n = 8$  mice; CNO,  $n = 8$  mice; Student t-test,  $p > 0.05$ ). **c** Excitation of PMd<sup>CCK</sup>-projecting mPFC neurons also did not affect the escape behavior in the presence of 15% CO<sub>2</sub> (Saline,  $n = 8$ ; CNO,  $n = 8$ ; Student t-test,  $p > 0.05$ ). **d** Schematic diagram of experimental design. **e** Exp I: chemogenetic inhibition of PMd<sup>CCK</sup>-projecting mPFC neurons during the escape-inducing assay period significantly decreased exaggerated flight behavior in the rat assay (left, both escape velocity and the number of climbs). Exp II: chemogenetic inhibition of PMd<sup>CCK</sup>-projecting mPFC neurons during the

conditioning period, the mice in the repeated group did not show exaggerated escape behavior in rat assays (right). (Saline,  $n = 8$  mice; CNO,  $n = 8$  mice; Student t-test, \*\*\* $p < 0.001$  and ns  $p > 0.05$ ). **f** Escape velocity and the number of flights for the same groups as in **(e)** during exposure to 15% CO<sub>2</sub>. Exp I: Inhibition of PMd<sup>CCK</sup>-projecting mPFC neurons during the escape-inducing assay period significantly decreased both escape velocity and the number of jumps. Exp II: Inhibition of PMd<sup>CCK</sup>-projecting mPFC neurons during the conditioning period, the mice did not show exaggerated flight behavior in CO<sub>2</sub> assays (right). (Saline,  $n = 8$  mice; CNO,  $n = 8$  mice; Student t-test, \*\*\* $p < 0.001$  ns  $p > 0.05$ ). **g** Model of a tripartite mPFC/VTg<sup>PV</sup> → PMd<sup>CCK</sup> synapses that utilizes eCB signal for heterosynaptic plasticity to control threat history-driven escape adaptation. Data are presented as means  $\pm$  SEM. See also Supplementary Fig. 6. Source data are provided as a Source Data file. CNO, Clozapine-N-oxide; Exp I, experiment I; Exp II, experiment II; GABA, gamma-aminobutyric acid.

behaviors elicited by predator threat<sup>62,63</sup>. Our results indicated that increased eCB signaling exacerbated the innate flight behaviors to high-imminence threats. With the widely used genetically encoded GPCR activation-based eCB biosensor (GRAB<sub>eCB2.0</sub>)<sup>34–39</sup>, we showed that the exaggerated flight was temporally coupled with increased eCB signal at the inhibitory VTg-PMd synapses (Fig. 5). And with precise genetic deletion of CB<sub>1</sub>R in the VTg axons, we subsequently demonstrated the necessity of the eCB signal for learning-induced escape strengthening. Together these studies suggest that the effect of eCB signaling on anxiety could potentially diverge due to different causes of the threats.

As mentioned previously, high-threat sensitivity is evolutionarily advantageous in dangerous environments for animals to quickly detect potential predators and escape from them. On the other hand, inappropriate activation of the same neural mechanism could cause panic disorder (PD) in humans<sup>64</sup>. While the etiology of PD is not completely understood, several brain regions involved in the escape behaviors are implicated<sup>64</sup>. Based on the anxiolytic effects of the eCBs, recent studies suggested that the eCB system could be a potential therapeutic target for treating anxiety<sup>65</sup>. However, animal studies using CB<sub>1</sub>R knockout, particularly in the GABAergic neurons, revealed that the eCB system has anxiogenic effects<sup>65</sup>. Similarly, pharmacological enhancement of the eCB signaling facilitated innate defensive behavior in high-threat environment<sup>62,65</sup>. Furthermore, increased risks for panic disorder have been associated with exogenous cannabinoid use in humans<sup>66,67</sup>. Thus, understanding the neural mechanism underlying the biphasic effect of eCB signaling on anxiety is critically important for its potential therapeutic application. Our study fills this gap of knowledge regarding the neural circuit mechanism of eCB signaling in strengthening defensive behavior. Considering that the neural circuits controlling escape overlap with those related to PD, the mechanism we discovered on eCB signaling may have implications for developing treatment for PD. Future studies are required to further dissect the neural mechanisms underlying the anxiolytic and anxiogenic effects of the eCB system under physiological escape behavior and pathological conditions.

## Methods

### Animals

All experiments were performed under the relevant guidelines of Fudan University and the National Institutes of Health Guidelines for the Care and Use of Laboratory Animals and were further approved by the Animal Advisory Committee at Fudan University.

### Mice

Male WT (C57BL/6), Cck-IRES-Cre (Jackson, strain name Cck<sup>tm1.1(crc)Zjh</sup>/J, stock number 012706), Pvalb-IRES-Cre (Jackson, strain name B6;129P2-Pvalb<sup>tm1(crc)Arbr</sup>/J, stock number 008069) and CAG-LSL-Cas9-tdTomato (GemPharmatech, strain name C57BL/6JGpt-Rosa26<sup>tm1(CAG-LSL-Cas9-tdTomato)</sup>/Gpt, stock number T002249) mice aged 8–14 weeks were used. Sample sizes were shown to be statistically powerful by estimating the variances of data from this study. All mice were housed under a 12 h light-dark cycle (lights on from 8:00 to 20:00) with food and water provided ad libitum. Holding and experimental room temperatures were maintained at 20–22 °C and humidity was maintained between 30% and 70%, with an average humidity of approximately 45%. All mice were randomly allocated into either the control or experimental group and were group-housed until surgery. After the surgical procedures, all experimental animals were single-housed. All behavioral tasks were performed during the light cycle.

### Rats

Male SD rats (250–400 g) aged 12–16 months were obtained from GemPharmatech and were individually housed on a standard 12-h light-dark cycle and given food and water ad libitum. Rats were only used as a predatory stimulus. No attacks on mice were observed in this experiment.

### Stereotaxic surgeries

Surgeries were performed as described previously<sup>12</sup>. Eight-week-old mice were anaesthetized with 1.5–3.0% isoflurane and placed in a stereotaxic apparatus (cat. nos. 68030, 68025, RWD life science). A scalpel was used to open an incision along the midline to expose the skull. After performing a craniotomy, 40–100 nl at a titer of  $\sim 2 \times 10^{12}$  particles/ml virus was injected per site. Injection sites were confirmed in all animals by preparing coronal sections (40  $\mu$ m) of injection sites after behavioral tests.

### Viral vectors

AAV(2/9)-EF1a-DIO-eGFP, AAV(2/9)-EF1a-fDIO-mCherry, Retro-AAV(2/2)-Flpo, AAV(2/9)-EF1a-DIO-hChR2(H134R)-mCherry, AAV(2/9)-syn-fDIO-ChrimsonR-tdTomato, AAV(2/8)-hSyn-DIO-hM3D(Gq)-mCherry, AAV(2/8)-CAG-DIO-GCaMP7s-WPRE-SV40, AAV(2/8)-hSyn-DIO-hM4D(Gi)-mCherry and AAV(2/9)-hSyn-DIO-hGtACR2-eGFP were prepared by the Shanghai Taitool Bioscience Co., Ltd. AAV(2/9)-EF1a-DIO-eCB2.0 was prepared by Brain Case (Shenzhen) Biotechnology Co., Ltd. The final titer was estimated to be  $\sim 10^{12}$  genome copies per milliliter. AAV (2/8)-CAG-DIO-TVA-eGFP ( $4.0 \times 10^{12}$ ), AAV (2/8)-CAG-DIO-rabies glycoprotein G ( $4.14 \times 10^{12}$ ), EnvA-G deleted rabies-DsRed and EnvA-G deleted rabies-Cre ( $3.0 \times 10^8$ ) were prepared by BrainVTA (Wuhan, China) Co., Ltd.

The *gRNA* (gCTGGATCATGCCAACTGCG) targeting *CB<sub>1</sub>R* were cloned to make AAV (2/9) - (H1-gRNA)  $\times$ 3-CAG-EGFP (*gRNA*, or AAV-*gRNAs*-EGFP for short,  $1.14 \times 10^{13}$  vg/ml, WZ Bio, Inc). In addition, viruses with scrambled *gRNAs* (*scram*) targeting the same gene sites (CCGGAAGAGCGAGCTCTTCT,  $1.20 \times 10^{13}$  vg/ml, WZ Bio, Inc) were made as controls.

### Viral injections and cannula implantation

Mice received unilateral 50–80 nl viral infusion using a nanoliter microinjection pump (RWD life science, R-480) and fiber optic cannula (200 mm OD, 0.22 NA, Inper Inc) implantation (0.15–0.3 mm above the viral injection coordinates). Infusion locations measured as anterior-posterior, medial-lateral, and dorsoventral coordinates from bregma were: dorsal premammillary nucleus (PMd, 80 nl,  $-2.46$  mm;  $\pm 0.5$  mm;  $-5.35$  mm), ventral tegmental nucleus of Gudden (VTg, 50 nl,  $-4.9$  mm;  $\pm 0.25$  mm;  $-3.90$  mm), medial prefrontal cortex (mPFC, 60 nl,  $1.8$  mm;  $\pm 0.5$  mm;  $-3.20$  mm). The injection glass capillary was withdrawn 10 min after the end of the infusion and the incision was closed with a suture. After implantation, all fibers were made to adhere to the skull with bone screws and dental cement. The animal was kept on a heating pad until fully recovered from anesthesia. Injection sites were confirmed in all animals by preparing coronal sections (50 or 100  $\mu$ m) of injection sites after behavioral tests.

For photometry experiments, mice were injected with 80 nl of AAV-DIO-GCaMP7s or AAV-DIO-eCB2.0 in the PMd or VTg, respectively of CCK-Cre or PV-Cre mice. Mice were implanted unilaterally with cannulas in the PMd. A 400  $\mu$ m diameter, 0.48 NA optical fiber (Inper Inc) was used for photometry experiments.

### In vivo fiber photometry recordings

Fiber photometry was applied to record  $\text{Ca}^{2+}$  signals or eCB signal<sup>12</sup>. Briefly, microinjections of the AAV-DIO-GCaMP7s virus were performed in the PMd and VTg, or injection of AAV-DIO-eCB2.0 virus was performed in the VTg, followed by implantation of an optical fiber, with mice allowed at least 3 weeks for recovery. A monofiber optic patch cord connected to the fiber photometry system (Inper) was attached to the implanted fiber optic cannula using a ceramic sleeve with black heat-shrinkable tubes. To record the fluorescence signals from GCaMP7s or eCB2.0, light from a 470-nm LED was bandpass-filtered (470/10 nm), collimated, reflected by dichroic mirrors, focused using a 20 $\times$  objective and delivered at 25–40  $\mu$ W from the tip of the fiber optic cannula. The emitted fluorescence from GCaMP7s or



eCB2.0 was bandpass-filtered (525/40 nm), focused on, and detected by the sensor of a complementary metal oxide semiconductor camera. The end of the fiber was imaged at a frame rate of 30 fps using the Inper Signal software; the mean value of the region of interest (ROI) at the end face of the fiber was calculated using Inper Plot software. Furthermore, a 410-nm LED light was bandpass-filtered and delivered alternately with a 470-nm LED light as an isosbestic control channel. GCaMP7s or eCB2.0 fluorescence intensity was then recorded. Fluorescence changes were quantified by  $\Delta F/F_0 = F(t) - F_0(t)/F_0(t)$  and the baseline was defined by the signals at 5 s before stimulus presentation. The Inper Plot software was applied to generate the average  $\text{Ca}^{2+}$  traces, with the shaded areas indicating the s.e.m.

### Optogenetic manipulation

All mice were handled daily for 3 days before the behavioral tasks. On the day of the experiment, mice were transported to a testing room and habituated for approximately 2 h. The chronically implanted fibers (diameter 200  $\mu\text{m}$ ) were connected to a laser generator via optic fiber sleeves, after which mice were returned to the home cage for at least 30 min. Next, either blue light (473 nm, ChR2: 2  $\text{mW}/\text{mm}^2$ , 5-ms pulses, 20 Hz; GtACR2: continuous light, 2  $\text{mW}/\text{mm}^2$ , Inper) was delivered to selectively activate or inhibit the soma and circuits under the control of an intelligent optogenetic system. After completion of all behavioral tests, mice were killed to verify the virus injection and optical fiber sites. Mice with missed injections or implantations were excluded from the study.

### Chemogenetics

Mice used for chemogenetic experiments were exposed to each threat and control stimuli twice, once following treatment with saline and once following treatment with CNO (LKT LABS, Cas No. 34233-69-7, 1–5  $\text{mg}/\text{kg}$ , injected intraperitoneally) 40 min before the experiment. Only one control or threat-exposure assay was performed per day with each mouse.

### Brain slice preparation

Acute brain slice preparations were performed. Mice were deeply anesthetized with pentobarbital sodium (2% w/v, intraperitoneal), then intracardially perfused with 20 ml of ice-cold oxygenated cutting solution (93 mM N-methyl-D-glucamine, 1.2 mM  $\text{NaH}_2\text{PO}_4$ , 2.5 mM KCl, 20 mM HEPES, 30 mM  $\text{NaHCO}_3$ , 2 mM thiourea, 25 mM glucose, 3 mM sodium pyruvate, 5 mM sodium ascorbate, 10 mM  $\text{MgSO}_4$ , 0.5  $\text{CaCl}_2$  and 3 mM glutathione (GSH)). Mice were then quickly decapitated and their brains were carefully removed from the skull. Each brain was glued on the bed plate of a vibratome and coronal slices (250  $\mu\text{m}$ ) containing the PMd or VTg were sliced in an ice-cold sucrose-based slicing solution, which is the normal artificial cerebrospinal fluid (aCSF) but with NaCl replaced by equimolar sucrose and sectioned at 0.1 mm s<sup>-1</sup> (VT1200s, Leica Biosystems). Slices were incubated in a cutting solution, and then immediately transferred into HEPES artificial cerebrospinal fluid (aCSF) (126 NaCl, 2.5 KCl, 2  $\text{MgSO}_4$ , 2  $\text{CaCl}_2$ , 26  $\text{NaHCO}_3$ , 1.25  $\text{NaH}_2\text{PO}_4$  and 25 dextrose) at 35.5 °C for 40–60 min and then placed at room temperature until recording. After incubation, slices were placed in a recording chamber (Warner Instruments) for electrophysiological recording with continuous perfusion of oxygenated standard aCSF, with the temperature maintained at 34 °C via an in-line solution heater (TC-344B, Warner Instruments). The aCSF pH was maintained within 7.3–7.4 and osmolarity was adjusted to 315 mOsm  $\text{kg}^{-1}$ . All solutions were continuously boiled with 95%  $\text{O}_2$  and 5%  $\text{CO}_2$  throughout slice preparation and electrophysiological recordings.

### In vitro electrophysiological recordings

Whole-cell patch-clamp recordings were performed on visualized PMd and VTg neurons using an infrared differential interference contrast (IR-DIC) microscope (BX-51WI, Olympus). For whole-cell recording at

VTg, the glass pipettes (5–7 M $\Omega$ ) were filled with intracellular solution (in mM, 140 K-Gluconate, 3 KCl, 2  $\text{MgCl}_2$ , 0.2 EGTA, 10 HEPES, 2  $\text{Na}_2\text{ATP}$ , (285–295 mOsm, pH 7.2)) for current-clamp recordings. Positive current pulses (10–100 pA per step, 500 ms in duration) and negative current pulses (–50 pA per step, 500 ms) were injected to examine the electrophysiological properties such as F-I curve when the cell was held at about –45 to –60 mV with no spontaneous firing.

To record light-evoked postsynaptic currents, glass pipettes had an impedance of 5–7 M $\Omega$  when filled with high-Cl<sup>–</sup> internal solution (72 K-Gluconate, 71 KCl, 2  $\text{MgCl}_2$ , 0.2 EGTA, 10 HEPES, 2  $\text{Na}_2\text{ATP}$ ) with osmolarity of 285–295 mOsm and pH 7.20–7.25. The blue light was delivered through a LED light source (473 nm, Fluca, FL0117) positioned above the surface of the target areas. The duration of each light pulse was 1 ms, and the intensity of continuous light output measured under the 40 $\times$  objective was 10 to 45 mW. The membrane potentials of neurons were held at –70 mV in voltage clamp to record IPSCs. Both recordings were immediately terminated once the series resistance reached above 10%. To eliminate polysynaptic components, TTX (1  $\mu\text{M}$ , Dalian Refine Biochemical Products) was applied to the standard aCSF to block the sodium channels. At the same time, 4-AP (200  $\mu\text{M}$ , Sigma-Aldrich) was added to augment light-induced postsynaptic currents. For all the recording, we employed a Multi-clamp 700B amplifier (Molecular Devices) and a Micro3 1401 analog-to-digital converter together with Spike2 software (version 8, Cambridge Electronic Design) for data acquisition.

### Behavioral Tests

**Rat exposure assay.** The behavioral paradigm had been described in our previous study<sup>12</sup>. Briefly, we used a corridor measuring (35  $\times$  20  $\times$  22 cm). There is a vertical wall with a wire mesh at the end of the corridor (with 1 cm  $\times$  1 cm square spaces in the mesh). Mice were acclimated to this environment for three days for 10 min. Mice freely explored and independently climbed up the grid ladder. The rat is restrained to the corner opposite the mesh grid by a harness attached to a string that is taped to the wall. Mice could climb to avoid the rat and hide in the burrow. After reaching the burrow mice were given 1 min of hiding time in the burrow. They were then gently placed back on the bottom floor of the context at the same level as the rat. The climb speed and number of climbs performed during 20 min were measured. This length of 20 min includes the 1-min hiding period in the burrow. The climb speed and number of climb entries into the shelter were analyzed offline using ANY-maze v7.0 (Stoelting Co.).

**Carbon dioxide exposure assay.** Animals were placed in a transparent box. Mice were acclimated to the environment for three days (10 min of exposure). The next day mice were exposed either to infusions of air or of 15%  $\text{CO}_2$ . The concentration of  $\text{CO}_2$  was measured and dynamically adjusted by the Pro $\text{CO}_2$  120 controller (Biospherix, USA) so that  $\text{CO}_2$  levels were maintained at 15%. This concentration of  $\text{CO}_2$  elicited escape jumps in all mice tested. The jump speed and number of jumps in 10 minutes were recorded. The jump speed and number of jumps were analyzed offline using ANY-maze v7.0 (Stoelting Co.).

**Conditioned place aversion procedures.** The CPA apparatus [62 cm (length)  $\times$  24 cm (width)  $\times$  24 cm (height)] made of Plexiglas was divided into two equal-sized compartments by a removable partition with an opening (8  $\times$  8 cm) at one end, which allowed mice ad libitum access to each compartment. Two compartments were distinguished by visual (white or black) and tactile cues (bar or slick) and provided distinct contexts that were paired with 2MT or saline. The apparatus was equipped with infrared photobeams connected to a computer that recorded the rat's location in the chambers.

To determine baseline place preference, the mice were initially placed in the apparatus with the doors removed for 15 min (pre-conditioning test). Conditioning was performed using an unbiased,

counterbalanced protocol, as described in our previous work<sup>68</sup>. Conditioning took place over the next 2 d. On the first day, the mice were confined to either compartment with saline in a counterbalanced manner for 20 min. On the second day, the mice were confined to the compartment with 2MT opposite to that on the first day for 20 min. This compartment will be referred to as the 2MT treatment-paired compartment. In the post-training testing phase (24 h after the conditioning trial), all mice were allowed to explore the entire apparatus for 10 min, and the amount of time spent in each compartment was recorded. CPA score represents the time in the drug treatment-paired compartment during the testing phase minus that during the pre-conditioning phase. Time spent in the compartment was analyzed offline using ANY-maze v7.0.

**Fluorescent retrobead retrograde tracing.** Mice were injected unilaterally with red fluorescent retrobeads (100 nl; LumaFluor Inc. #78R170) into the PMd (AP: −2.46 mm; ML: ±0.5 mm; DV: −5.35 mm). The incision was closed with a suture and a tissue adhesive and the animal was kept on a heating pad until it recovered from anesthesia.

**Rabies tracing.** The strategy builds on the targeting of Cre-dependent co-expression of the avian receptor TVA and the rabies glycoprotein G (RVG) on principle neurons through injection of helper viruses (AAV-CAG-DIO-TVA-eGFP and AAV-CAG-DIO-RVG) into the PMd (AP: −2.46 mm; ML: 0.5 mm; DV: −5.35 mm) of CCK-IRES-Cre mice on day 1. A genetically modified rabies virus (RV) pseudotyped with the avian envelope protein was delivered to the same coordinates on day 21 after the injection of helper viruses. Given that RV lacks an endogenous gene of RVG and has been genetically modified to express the fluorescent protein dsRed, the RV can only infect cells expressing the TVA while further spread of the rabies virus is limited due to the deletion of RVG. 7 days after RV injection, mice were perfused with 4% PFA in PBS. Brains were stored in 30% sucrose in PBS at 4 °C overnight and then 40 µm slices were collected for imaging by using an Olympus microscope (VS200).

**Immunostaining for NeuN, Fos and CB<sub>1</sub>R.** Animals were perfused, fixed brains were kept in 30% sucrose, and the brains were sectioned on a sliding microtome in the frontal plane (Leica CM 1950). Sections were rinsed in 0.01 M PBS (pH = 7.2) with 10 min × 3 times and transferred sections into 0.3% (v/v) Triton-X 100 in PBS and incubated for 30 min (room temperature, RT). After PBS rinsing, sections were blocked with 5% (w/v) normal bovine serum for 1 h at RT or 4 °C overnight and then were incubated with primary antibodies overnight in 4 °C: Anti-cfos (1:1000, rabbit, abcam, ab190289), Anti-NeuN antibody (1:500, rabbit, Novusbio, NBP1-77686SS) or Anti-CB<sub>1</sub>R (1:500, rabbit, Frontier Institute, MSFR100580). The next day, brain sections were stained for 2 h in secondary antibodies (1:1000, abcam, ab150083, Alexa Fluor 594 goat anti-rabbit). Antibodies were diluted in phosphate-buffered saline which contained 2% (w/v) BSA and 0.3% (v/v) Triton X-100. Sections were washed in PBS 3 times for 10 min, incubated with DAPI (1/50000 dilution in PBS, Invitrogen), washed again in PBS, and mounted under coverslips with Fluoromount Aqueous Mounting Medium (Sigma-Aldrich). Image acquisition was performed with Olympus VS200 laser scanning microscope or Evident FV3000 using 20× or 40× objectives. Confocal images were analyzed using ImageJ.

**RT-PCR.** RT-PCR was performed as described previously. Cytoplasm from ventral tegmental nucleus of Gudden of PV<sup>Cre</sup>::Cas9<sup>fl</sup> mouse with control or gRNA virus injection after behavioral test. Harvested mRNA was first reverse transcribed to cDNA using a Super Script III kit (Invitrogen, USA), incubated at 50 °C for 50 min, and then terminated at 65 °C for 20 min. The entire cDNA was then amplified by multiplex PCR for 25 cycles (94 °C for 40 s, 57 °C for 90 s, 72 °C for 60 s, and a final

extension at 72 °C for 10 min) using a QIAGEN Multiplex PCR Master Mix kit (QIAGEN, Germany) in a 100 µL volume. The transcripts of each tested gene were detected by a second round of PCR using an individual primer set: 1 µL of the multiplex PCR mixture was applied as a template in a 10 µL reaction with HotStarTaq polymerase (TianGen, China) and cycled again (35 cycles of 94 °C for 40 s, 57 °C for 40 s, 72 °C for 60 s, and a final extension at 72 °C for 10 min). The PCR products were run on a 2% agarose gel stained with GelRed (Invitrogen, USA) and visualized with ultraviolet light. The identities of the amplicons were confirmed by DNA sequencing (Sangon Biotech, China). Primers for GAPDH and CB<sub>1</sub>R were designed according to NCBI published sequences, as follows: CB<sub>1</sub>R (295 bp): Forward 50-AGGA-GAACGAGGACAACA-30, Reverse 30-ACATTGGGACTATCTTTGC-50; GAPDH (572 bp): Forward 50-ACTCCACTCACGGCAAATTC-30, Reverse 30-CACATTGGGGTAGGAACAC-50; To avoid false negatives, only PCR detections of GAPDH were counted.

### Imaging and analysis

Whole-brain slides were imaged using a ×20 magnification on an Olympus VS 200 virtual slide microscope system or Evident FV3000 and processed with ImageJ. The placement of the optical fibers was assessed based on the lesions in the tissues produced by the fiber tips. The expression levels of virus-infected cell bodies and axons were outlined in the corresponding sections in the mouse brain stereotaxic coordinates. We use Simple Neurite Tracer's moniker (SNT)<sup>69</sup>, which is very well integrated with the ImageJ platform to trace and reconstruct the expression of CB<sub>1</sub>R along dendrites (Fig. 7).

### Statistical analysis

Two-tailed student's paired t-tests or unpaired t-tests, and one- or two-way ANOVA tests were used to determine statistical differences for anatomical, behavioral, and electrophysiological data using GraphPad Prism 10 (GraphPad Software). Post hoc analysis was applied when ANOVA showed a significant main effect. Raw data as shown in Supplementary Dataset, related to Figs. 1, 2, 3, 4, 5, 6, 7, S1, S2, S3, S4, S5, and S6. \**p* < 0.05, \*\**p* < 0.01, \*\*\**p* < 0.001. All data are presented as means ± SEM.

### Reporting summary

Further information on research design is available in the Nature Portfolio Reporting Summary linked to this article.

### Data availability

The datasets generated and/or analyzed during the current study can be found in the paper and the supplementary materials. Any additional research materials will be made available on a request at weishengw@fudan.edu.cn. Source data are provided with this paper.

### Code availability

No original code was generated in this study.

### References

1. Tseng, Y. T., Schaefke, B., Wei, P. & Wang, L. Defensive responses: behaviour, the brain and the body. *Nat. Rev. Neurosci.* **24**, 655–671 (2023).
2. Cooper, W. E. Jr. Optimal escape theory predicts escape behaviors beyond flight initiation distance: risk assessment and escape by striped plateau lizards *Sceloporus virgatus*. *Curr. Zool.* **55**, 123–131 (2009).
3. Hawlena, D., Kress, H., Dufresne, E. R. & Schmitz, O. J. Grasshoppers alter jumping biomechanics to enhance escape performance under chronic risk of spider predation. *Funct. Ecol.* **25**, 279–288 (2011).
4. Freymiller, G. A., Whitford, M. D., Higham, T. E. & Clark, R. W. Recent interactions with snakes enhance escape performance of desert

- kangaroo rats (Rodentia: Heteromyidae) during simulated attacks. *Biol. J. Linn. Soc.* **122**, 651–660 (2017).
5. Bateman, P. W. & Fleming, P. A. Switching to Plan B: changes in the escape tactics of two grasshopper species (Acrididae: Orthoptera) in response to repeated predatory approaches. *Behav. Ecol. Sociobiol.* **68**, 457–465 (2014).
  6. Wooster, E. I. F. et al. Animal cognition and culture mediate predator-prey interactions. *Trends Ecol. Evol.* **39**, 52–64 (2024).
  7. Gross, C. T. & Canteras, N. S. The many paths to fear. *Nat. Rev. Neurosci.* **13**, 651–658 (2012).
  8. Tovote, P. et al. Midbrain circuits for defensive behaviour. *Nature* **534**, 206–212 (2016).
  9. Evans, D. A. et al. A synaptic threshold mechanism for computing escape decisions. *Nature* **558**, 590–594 (2018).
  10. Deng, H., Xiao, X. & Wang, Z. Periaqueductal gray neuronal activities underlie different aspects of defensive behaviors. *J. Neurosci.* **36**, 7580–7588 (2016).
  11. Wang, W. et al. Dorsal premammillary projection to periaqueductal gray controls escape vigor from innate and conditioned threats. *Elife* **10** (2021).
  12. Wang, W. et al. Coordination of escape and spatial navigation circuits orchestrates versatile flight from threats. *Neuron* **109**, 1848–1860 e1848 (2021).
  13. Wickersham, I. R., Finke, S., Conzelmann, K. K. & Callaway, E. M. Retrograde neuronal tracing with a deletion-mutant rabies virus. *Nat. Methods* **4**, 47–49 (2007).
  14. Qi, S. et al. How cognitive and reactive fear circuits optimize escape decisions in humans. *Proc. Natl. Acad. Sci. USA* **115**, 3186–3191 (2018).
  15. Tomsic, D., de Astrada, M. B., Sztarker, J. & Maldonado, H. Behavioral and neuronal attributes of short- and long-term habituation in the crab *Chasmagnathus*. *Neurobiol. Learn Mem.* **92**, 176–182 (2009).
  16. Comoli, E., Ribeiro-Barbosa, E. R. & Canteras, N. S. Afferent connections of the dorsal premammillary nucleus. *J. Comp. Neurol.* **423**, 83–98 (2000).
  17. Gongwer, M. W. et al. Brain-wide projections and differential encoding of prefrontal neuronal classes underlying learned and innate threat avoidance. *J. Neurosci.* **43**, 5810–5830 (2023).
  18. McNaughton, N. & Vann, S. D. Construction of complex memories via parallel distributed cortical-subcortical iterative integration. *Trends Neurosci.* **45**, 550–562 (2022).
  19. Yan, J. J. et al. A circuit from the ventral subiculum to anterior hypothalamic nucleus GABAergic neurons essential for anxiety-like behavioral avoidance. *Nat. Commun.* **13**, 7464 (2022).
  20. Xie, Z. et al. Mechanically evoked defensive attack is controlled by GABAergic neurons in the anterior hypothalamic nucleus. *Nat. Neurosci.* **25**, 72–85 (2022).
  21. Wang, L., Chen, I. Z. & Lin, D. Collateral pathways from the ventromedial hypothalamus mediate defensive behaviors. *Neuron* **85**, 1344–1358 (2015).
  22. Whittle, N. et al. Central amygdala micro-circuits mediate fear extinction. *Nat. Commun.* **12**, 4156 (2021).
  23. Klein, A. S., Dolensek, N., Weiand, C. & Gogolla, N. Fear balance is maintained by bodily feedback to the insular cortex in mice. *Science* **374**, 1010–1015 (2021).
  24. Dillingham, C. M. et al. Calcium-binding protein immunoreactivity in Gudden's tegmental nuclei and the hippocampal formation: differential co-localization in neurons projecting to the mammillary bodies. *Front. Neuroanat.* **9**, 103 (2015).
  25. Zhou, Z. et al. A VTA GABAergic neural circuit mediates visually evoked innate defensive responses. *Neuron* **103**, 473–488 e476 (2019).
  26. Venkataraman, A. et al. Modulation of fear generalization by the zona incerta. *Proc. Natl. Acad. Sci. USA* **116**, 9072–9077 (2019).
  27. Ahmadlou, M. et al. A cell type-specific cortico-subcortical brain circuit for investigatory and novelty-seeking behavior. *Science* **372** (2021).
  28. Fratzl, A. et al. Flexible inhibitory control of visually evoked defensive behavior by the ventral lateral geniculate nucleus. *Neuron* **109**, 3810–3822 e3819 (2021).
  29. Evans, D. A., Stempel, A. V., Vale, R. & Branco, T. Cognitive control of escape behaviour. *Trends Cogn. Sci.* **23**, 334–348 (2019).
  30. Dudok, B. et al. Retrograde endocannabinoid signaling at inhibitory synapses in vivo. *Science* **383**, 967–970 (2024).
  31. Freund, T. F. & Hajos, N. Excitement reduces inhibition via endocannabinoids. *Neuron* **38**, 362–365 (2003).
  32. Castillo, P. E., Younts, T. J., Chavez, A. E. & Hashimoto, Y. Endocannabinoid signaling and synaptic function. *Neuron* **76**, 70–81 (2012).
  33. Wittmann, G. et al. Distribution of type 1 cannabinoid receptor (CB1)-immunoreactive axons in the mouse hypothalamus. *J. Comp. Neurol.* **503**, 270–279 (2007).
  34. Farrell, J. S. et al. In vivo endocannabinoid dynamics at the time-scale of physiological and pathological neural activity. *Neuron* **109**, 2398–2403 e2394 (2021).
  35. Gunduz-Cinar, O. et al. A cortico-amygdala neural substrate for endocannabinoid modulation of fear extinction. *Neuron* **111**, 3053–3067 e3010 (2023).
  36. Liput, D. J. et al. 2-Arachidonoylglycerol mobilization following brief synaptic stimulation in the dorsal lateral striatum requires glutamatergic and cholinergic neurotransmission. *Neuropharmacology* **205**, 108916 (2022).
  37. Kondev, V. et al. Endocannabinoid release at ventral hippocampal-amygdala synapses regulates stress-induced behavioral adaptation. *Cell Rep.* **42**, 113027 (2023).
  38. Dong, A. et al. A fluorescent sensor for spatiotemporally resolved imaging of endocannabinoid dynamics in vivo. *Nat. Biotechnol.* **40**, 787–798 (2022).
  39. Liu, Z. et al. Deficiency in endocannabinoid synthase DAGLB contributes to early onset Parkinsonism and murine nigral dopaminergic neuron dysfunction. *Nat. Commun.* **13**, 3490 (2022).
  40. Hashimoto, Y., Ohno-Shosaku, T. & Kano, M. Ca(2+)-assisted receptor-driven endocannabinoid release: mechanisms that associate presynaptic and postsynaptic activities. *Curr. Opin. Neurobiol.* **17**, 360–365 (2007).
  41. Ritter, A., Habusha, S., Givon, L., Edut, S. & Klavir, O. Prefrontal control of superior colliculus modulates innate escape behavior following adversity. *Nat. Commun.* **15**, 2158 (2024).
  42. Miller, E. K. & Cohen, J. D. An integrative theory of prefrontal cortex function. *Annu. Rev. Neurosci.* **24**, 167–202 (2001).
  43. Armbruster, B. N., Li, X., Pausch, M. H., Herlitze, S. & Roth, B. L. Evolving the lock to fit the key to create a family of G protein-coupled receptors potentially activated by an inert ligand. *Proc. Natl. Acad. Sci. USA* **104**, 5163–5168 (2007).
  44. Zhang, S. et al. Molecular basis for selective activation of DREADD-based chemogenetics. *Nature* **612**, 354–362 (2022).
  45. Vann, S. D. Gudden's ventral tegmental nucleus is vital for memory: re-evaluating diencephalic inputs for amnesia. *Brain* **132**, 2372–2384 (2009).
  46. Bassant, M. H. & Poindessous-Jazat, F. Ventral tegmental nucleus of Gudden: a pontine hippocampal theta generator?. *Hippocampus* **11**, 809–813 (2001).
  47. Vann, S. D. Dismantling the Papez circuit for memory in rats. *Elife* **2**, e00736 (2013).
  48. Friedman, N. P. & Robbins, T. W. The role of prefrontal cortex in cognitive control and executive function. *Neuropsychopharmacology* **47**, 72–89 (2022).



49. Koechlin, E. Prefrontal executive function and adaptive behavior in complex environments. *Curr. Opin. Neurobiol.* **37**, 1–6 (2016).
50. Sangha, S., Diehl, M. M., Bergstrom, H. C. & Drew, M. R. Know safety, no fear. *Neurosci. Biobehav. Rev.* **108**, 218–230 (2020).
51. Soltani, A. & Koechlin, E. Computational models of adaptive behavior and prefrontal cortex. *Neuropsychopharmacology* **47**, 58–71 (2022).
52. Borkar, C. D. et al. Top-down control of flight by a non-canonical cortico-amygdala pathway. *Nature* **625**, 743–749 (2024).
53. Chou, X. L. et al. Inhibitory gain modulation of defense behaviors by zona incerta. *Nat. Commun.* **9**, 1151 (2018).
54. Hanganu-Opatz, I. L. et al. Resolving the prefrontal mechanisms of adaptive cognitive behaviors: A cross-species perspective. *Neuron* **111**, 1020–1036 (2023).
55. Moscarello, J. M. & Penzo, M. A. The central nucleus of the amygdala and the construction of defensive modes across the threat-imminence continuum. *Nat. Neurosci.* **25**, 999–1008 (2022).
56. Izquierdo, I., Furini, C. R. & Myskiw, J. C. Fear Memory. *Physiol. Rev.* **96**, 695–750 (2016).
57. Moscarello, J. M. & Maren, S. Flexibility in the face of fear: Hippocampal-prefrontal regulation of fear and avoidance. *Curr. Opin. Behav. Sci.* **19**, 44–49 (2018).
58. Patel, S., Hill, M. N., Cheer, J. F., Wotjak, C. T. & Holmes, A. The endocannabinoid system as a target for novel anxiolytic drugs. *Neurosci. Biobehav. Rev.* **76**, 56–66 (2017).
59. Lutz, B., Marsicano, G., Maldonado, R. & Hillard, C. J. The endocannabinoid system in guarding against fear, anxiety and stress. *Nat. Rev. Neurosci.* **16**, 705–718 (2015).
60. Chadwick, V. L., Rohleder, C., Koethe, D. & Leweke, F. M. Cannabinoids and the endocannabinoid system in anxiety, depression, and dysregulation of emotion in humans. *Curr. Opin. Psychiatry* **33**, 20–42 (2020).
61. Kondev, V. et al. The endocannabinoid 2-Arachidonoylglycerol Bidirectionally Modulates Acute and Protracted Effects of Predator Odor Exposure. *Biol. Psychiatry* **92**, 739–749 (2022).
62. Heinz, D. E., Genewsky, A. & Wotjak, C. T. Enhanced anandamide signaling reduces flight behavior elicited by an approaching robo-beetle. *Neuropharmacology* **126**, 233–241 (2017).
63. Uribe-Marino, A. et al. Anti-aversive effects of cannabidiol on innate fear-induced behaviors evoked by an ethological model of panic attacks based on a prey vs the wild snake *Epicrates cenchria crassus* confrontation paradigm. *Neuropsychopharmacology* **37**, 412–421 (2012).
64. Guan, X. & Cao, P. Brain mechanisms underlying panic attack and panic disorder. *Neurosci. Bull.* **40**, 795–814 (2024).
65. Petrie, G. N., Nastase, A. S., Aukema, R. J. & Hill, M. N. Endocannabinoids, cannabinoids and the regulation of anxiety. *Neuropharmacology* **195**, 108626 (2021).
66. Patton, G. C. et al. Cannabis use and mental health in young people: cohort study. *BMJ* **325**, 1195–1198 (2002).
67. Gorelick, D. A. Cannabis-related disorders and toxic effects. *N. Engl. J. Med.* **389**, 2267–2275 (2023).
68. Wang, W. S. et al. Extinction of aversive memories associated with morphine withdrawal requires ERK-mediated epigenetic regulation of brain-derived neurotrophic factor transcription in the rat ventromedial prefrontal cortex. *J. Neurosci.* **32**, 13763–13775 (2012).
69. Arshadi, C., Gunther, U., Eddison, M., Harrington, K. I. S. & Ferreira, T. A. SNT: a unifying toolbox for quantification of neuronal anatomy. *Nat. Methods* **18**, 374–377 (2021).

## Acknowledgements

We thank Profs. Peng Yuan (Fudan University) and Hongbin Yang (Zhejiang University) for helpful discussions. We were supported by grants from the STI2030-Major Projects (2021ZD0202703 to W.W.) and National Natural Science Foundation of China (NNSF32271067 to W.W. NNSF 82371527 to X.H.); We thank Profs. B. Song for providing rats.

## Author contributions

Conceptualization, R.C. and W.W.; Methodology, R.C. and W.W.; behavioral tests and viral injections, R.C., N.W., J.N., L.L., Z.X., S.D.; immunohistochemistry studies, H.W., M.L., R.G., H.L., X. G; Electrophysiological studies, Z.X.; Perfusion, R.W., Z.L.; Virus generation, S.Z.; Writing—Original Draft, H.H. and W.W.; Writing—Review & Editing, W.W. and X.-H.X.; Funding Acquisition, X.H. and W.W.; Resources, T.-L.C. and Y.S.; Supervision, W.W.

## Competing interests

The authors declare no competing interests.

## Additional information

**Supplementary information** The online version contains supplementary material available at <https://doi.org/10.1038/s41467-025-60080-1>.

**Correspondence** and requests for materials should be addressed to Yousheng Shu, Huilin Hong, Xiao Huang or Weisheng Wang.

**Peer review information** *Nature Communications* thanks the anonymous reviewers for their contribution to the peer review of this work. [A peer review file is available.]

**Reprints and permissions information** is available at <http://www.nature.com/reprints>

**Publisher's note** Springer Nature remains neutral with regard to jurisdictional claims in published maps and institutional affiliations.

**Open Access** This article is licensed under a Creative Commons Attribution-NonCommercial-NoDerivatives 4.0 International License, which permits any non-commercial use, sharing, distribution and reproduction in any medium or format, as long as you give appropriate credit to the original author(s) and the source, provide a link to the Creative Commons licence, and indicate if you modified the licensed material. You do not have permission under this licence to share adapted material derived from this article or parts of it. The images or other third party material in this article are included in the article's Creative Commons licence, unless indicated otherwise in a credit line to the material. If material is not included in the article's Creative Commons licence and your intended use is not permitted by statutory regulation or exceeds the permitted use, you will need to obtain permission directly from the copyright holder. To view a copy of this licence, visit <http://creativecommons.org/licenses/by-nc-nd/4.0/>.

© The Author(s) 2025

<sup>1</sup>Department of Neurology, Jinshan Hospital, Institute for Translational Brain Research, State Key Laboratory of Brain Function and Disorders, MOE Frontiers Center for Brain Science, Fudan University, Shanghai 201508, China. <sup>2</sup>Department of Psychological Medicine, Zhongshan Hospital, Fudan University, Shanghai 200032, China. <sup>3</sup>Institute of Pediatrics, National Children's Medical Center, Children's Hospital, Institute for Translational Brain Research, State Key

Laboratory of Brain Function and Disorders, MOE Frontiers Center for Brain Science, Fudan University, Shanghai 200032, China. <sup>4</sup>Institute for Brain Science, State Key Laboratory of Brain Function and Disorders, MOE Frontiers Center for Brain Science, Fudan University, Shanghai 200032, China. <sup>5</sup>Institute for Translational Brain Research, State Key Laboratory of Brain Function and Disorders, MOE Frontiers Center for Brain Science, Fudan University, Shanghai 200032, China. <sup>6</sup>These authors contributed equally: Ruikai Chai, Nawen Wang, Jinlu Nie, Zongyi Xu. ✉e-mail: [yousheng@fudan.edu.cn](mailto:yousheng@fudan.edu.cn); [hlhong1001@hotmail.com](mailto:hlhong1001@hotmail.com); [huang.xiao@zs-hospital.sh.cn](mailto:huang.xiao@zs-hospital.sh.cn); [weishengw@fudan.edu.cn](mailto:weishengw@fudan.edu.cn)